International Journal of Solids and Structures 326 (2026) 113779

Contents lists available at ScienceDirect

International Journal of Solids and Structures

journal homepage: www.elsevier.com/locate/ijsolstr

A microstructure-informed hyperelastic model for CNT-based polymer nanocomposites under large deformations

Matteo Pelliciari *, Stefano Sirotti, Angelo Marcello Tarantino

DIEF, Department of Engineering "Enzo Ferrari", via P. Vivarelli 10, 41125 Modena, Italy

ARTICLE INFO

Keywords:
Nonlinear elasticity
Strain energy function
Carbon nanotubes
Elastomers
Agglomeration
Softening

ABSTRACT

Modeling the mechanical response of carbon nanotube (CNT)-reinforced polymer nanocomposites (PNCs) under large deformations remains an open and complex challenge. Microstructural phenomena such as the formation of CNT agglomerates and the progressive detachment of CNTs from the polymer matrix significantly influence the macroscopic mechanical behavior, particularly in the nonlinear regime. These effects are further complicated by variability introduced during fabrication, which can significantly affect both internal morphology and mechanical performance. Despite progress in the field, a comprehensive hyperelastic model capable of capturing these phenomena and linking them to continuum-level response is still lacking. This work presents a physically motivated hyperelastic model informed by scanning electron microscopy (SEM) observations. The growth of agglomerates and the local increase in CNT concentration are incorporated using functions derived from underlying statistical distributions. The reinforcement contributions of CNTs in agglomerated and non-agglomerated regions are described by strain energy functions reflecting microstructural observations. Interfacial detachment is captured within the framework of *continuous* softening hyperelasticity, introducing *critical strain invariants* to define the onset of debonding. All model parameters retain a clear physical interpretation and can be directly estimated from SEM imaging, making the model fully predictive without requiring mechanical test data. To demonstrate practical applicability, the model is implemented in a finite element framework and validated against experimental simple tension and bending tests. Additionally, a simplified version of the model is proposed for cases where microstructural data are unavailable, following a more classical phenomenological approach in nonlinear mechanics. This formulation requires only stress–strain data for calibration and is shown to accurately reproduce experimental results from three independent datasets, confirming the effectiveness and versatility of the proposed approach.

1. Introduction

Polymeric materials, and particularly elastomers, are capable of undergoing large reversible deformations. This unique mechanical behavior makes them indispensable in a wide range of modern technologies. From biomedical implants and wearable devices (Guimard et al., 2007) to soft robotic components (Gorissen et al., 2019; Chen et al., 2019), stretchable electronics (Stewart and Sitaraman, 2021; Liu et al., 2021; Zhao et al., 2025), and impact-resistant systems (Du Bois et al., 2006), polymers play a central role in enabling flexible, lightweight, and resilient designs. Despite these advantages, their widespread use is often constrained by their relatively low stiffness and limited load-bearing capacity compared to other engineering materials, such as metals or ceramics. Moreover, the intrinsically insulating nature of most polymers poses challenges for their integration into electronic and sensing platforms (Corzo et al., 2020). As a result, efforts to overcome these drawbacks began in the early decades of the 20th century through the incorporation of rigid fillers such as carbon black and silica, which provided a means to enhance mechanical performance and improve electrical conductivity (Yamaguchi et al., 2003; Lorenz and Klüppel, 2012; Zhang et al., 2023).

The advent of carbon nanotubes (CNTs) has enabled the development of a new class of high-performance fillers for polymer-based materials. When dispersed within a polymer matrix, these nanoscale inclusions give rise to what are known as polymer nanocomposites (PNCs). Thanks to their extraordinary mechanical strength, electrical conductivity, and high surface-to-volume ratio, CNTs can drastically enhance the properties of the host polymer even at low loadings (Moniruzzaman and Winey, 2006; Kim et al., 2010; Fu et al., 2019; Matos et al., 2018). Qian et al. (2000) observed that the addition of just 1 wt% CNTs to polystyrene improved tensile strength by 25% and

* Corresponding author.
E-mail addresses: matteo.pelliciari@unimore.it (M. Pelliciari), stefano.sirotti@unimore.it (S. Sirotti), angelomarcello.tarantino@unimore.it (A.M. Tarantino).

https://doi.org/10.1016/j.ijsolstr.2025.113779
Received 28 July 2025; Received in revised form 12 November 2025; Accepted 17 November 2025
Available online 17 November 2025

elastic stiffness by 40%. Cha et al. (2017) reported a 64% increase in Young's modulus and a 22% rise in ultimate tensile strength in epoxy-based PNCs reinforced with 2 wt% CNTs. Enhancements are not limited to mechanical performance. Functional properties such as electrical and thermal conductivity also benefit considerably. Winey et al. (2007) demonstrated an increase in electrical conductivity from 10^{-5} S/cm to 1 S/cm in polystyrene reinforced with 10 wt% single-walled CNTs. Zhang et al. (2019) produced CNT-based PNCs reaching an electrical conductivity of 2.1×10^3 S/cm, marking a transition from insulating to truly conductive behavior. Owing to these multifunctional improvements, PNCs have emerged as promising materials for advanced technologies, including flexible sensors (Qin et al., 2015), gas barrier coatings (Cui et al., 2016), self-healing systems (Thakur and Kessler, 2015), energy storage devices (Wang and Zhu, 2011), and membranes (Miculescu et al., 2016; Bassyouni et al., 2019).

Incorporating CNTs into polymer matrices presents several challenges, the most relevant of which are summarized below. First, CNTs have a strong tendency to form agglomerates, which can significantly affect the mechanical performance of the composite. Several studies have shown that agglomeration leads to premature damage onset, reduced stress transfer efficiency, diminished stiffening contribution from the CNTs, and lower ultimate strain (Romanov et al., 2015; Zare et al., 2017; Moradi et al., 2025; Matveeva et al., 2019; Abhiram and Ghosh, 2023). The extent of agglomeration depends on both the CNT type and the processing method used to fabricate the PNC (Moon et al., 2014; Moreira et al., 2010). Second, the interaction between CNTs and the polymer matrix has a major influence on the mechanical behavior of the composite. A sufficiently strong interfacial bond is important for effective load transfer, as a weak interface greatly reduces the reinforcing potential of CNTs (Cooper et al., 2002). This interaction depends on several factors, including surface chemistry, dispersion state, and polymer chain mobility (Senses and Akcora, 2013; Shen et al., 2014; Molinari et al., 2018; Rahmat and Hubert, 2011; Jiang et al., 2006). Finally, the reinforcing effect provided by CNTs is not constant but evolves with deformation, particularly under large strains. Although an initial increase in stiffness is always observed, this effect typically diminishes as strain increases, due to debonding at the CNT-matrix interface. Frogley et al. (2003) reported that most of the stiffness enhancement in silicone-based elastomers containing single-walled CNTs is lost beyond 10%–20% strain. Additionally, interfacial degradation leads to reduced failure strain, as observed by Dufresne et al. (2002), Koerner et al. (2005), and Xing et al. (2014). The above aspects make the modeling of the mechanical response of CNT-based PNCs particularly challenging, and indeed, it remains an open problem in the current scientific literature.

The behavior of conventional polymers under large elastic deformations has been widely studied, with extensive research dedicated to developing hyperelastic models within the framework of nonlinear elasticity. In the case of PNCs, however, the formulation of hyperelastic models capable of capturing their large-deformation behavior remains a significant challenge. Most hyperelastic models developed for polymers are phenomenological in nature and rely on parameter fitting to experimental stress–strain data. One of the earliest and most influential contributions in this context is the generalized Rivlin model (Rivlin and Saunders, 1951). Building on this foundation, several other models have been introduced, including the Yeoh and Yeoh–Fleming models (Yeoh, 1990; Yeoh and Fleming, 1997), the Gent and Gent–Gent models (Gent, 1996; Pucci and Saccomandi, 2002), and the Ogden model (Ogden, 1972). While these models are effective for polymers, they are generally inadequate for PNCs. This is because the mechanical response of PNCs is highly sensitive to changes in nanofiller content, geometry, and dispersion state. As a result, the parameters fitted in a given formulation cannot be generalized across systems with different filler characteristics, limiting the predictive value of such models. Therefore, the development of hyperelastic formulations that are applicable to PNCs and consistent with experimental observations remains an open area of research.

Among the limited efforts in the literature aimed at modeling PNCs within the framework of nonlinear elasticity, Cantournet et al. (2007) reinforced an elastomer with multi-walled CNTs and proposed a hyperelastic model based on the rule of mixtures. The investigated nanocomposites exhibited failure at relatively low strains, and thus nonlinear effects associated with large deformations, such as CNT debonding, were not observed. CNT agglomeration was also not considered. Shin et al. (2019) and Arash et al. (2019, 2021) proposed multiscale homogenization-based hyperelastic models for PNCs, calibrated through molecular dynamics (MD) simulations. Their studies, which focused on nanoparticle-reinforced epoxy nanocomposites, considered materials subjected to relatively small deformations, with strains up to 6%–8% in simple tension. Islam et al. (2023) developed a multiscale continuum model for polymers reinforced with nanofibers, also calibrated using MD simulations. Their formulation does not account for CNT agglomeration and its influence on mechanical response. Other studies have employed classical hyperelastic models, fitting parameters directly to experimental data on PNCs, without distinguishing between the contributions of the matrix and nanofillers (Barghamadi et al., 2021; He et al., 2022).

Based on the above discussion, several limitations can be identified in the current modeling approaches for PNCs in nonlinear elasticity. First, there is a lack of models that establish a direct connection between the internal morphology of the nanocomposite and its macroscopic mechanical response. In particular, current models do not yet incorporate the effects of CNT agglomeration on nonlinear stress response in a clear and systematic way. Second, existing models generally fall short in representing the progressive detachment of CNTs from the polymer matrix under large deformations. A physically grounded approach that accounts for this effect, while remaining practical for engineering applications, is still lacking. Finally, there remains a strong need for a versatile model capable of reproducing the experimentally observed stress–strain behavior of PNCs. As noted earlier, the mechanical response of PNCs is highly sensitive to differences in fabrication methods, which can lead to substantial variability even when the same polymer matrix and nanofiller type are employed. Therefore, it is essential to develop constitutive models that can be calibrated either from morphological observations (e.g., SEM imaging) or from mechanical test data of the specific PNC under consideration. The model parameters should retain a clear physical interpretation, such as those linked to CNT agglomeration and interfacial detachment.

In the present work, we address the above limitations by proposing a hyperelastic model for CNT-based PNCs with the following advancements.

- The presence of agglomerates, as well as the locally increased concentration of CNTs within these regions, is quantified through SEM investigations. Their progressive formation is incorporated into the hyperelastic formulation, with a dedicated term that captures their influence on the macroscopic stress response.
- The contribution of CNT-matrix detachment at large strains is analyzed via SEM imaging of stretched specimens and is introduced into the model through a physically motivated form of the strain energy function (SEF).
- The predictive capability and practical applicability of the proposed model are demonstrated through validation against experimental data from simple tension tests, followed by finite element (FE) implementation and application to PNC beams subjected to three-point bending. The numerical results obtained from the FE analyses demonstrate that the model is versatile and accurately reproduces the experimental data from bending tests on PNC beams.

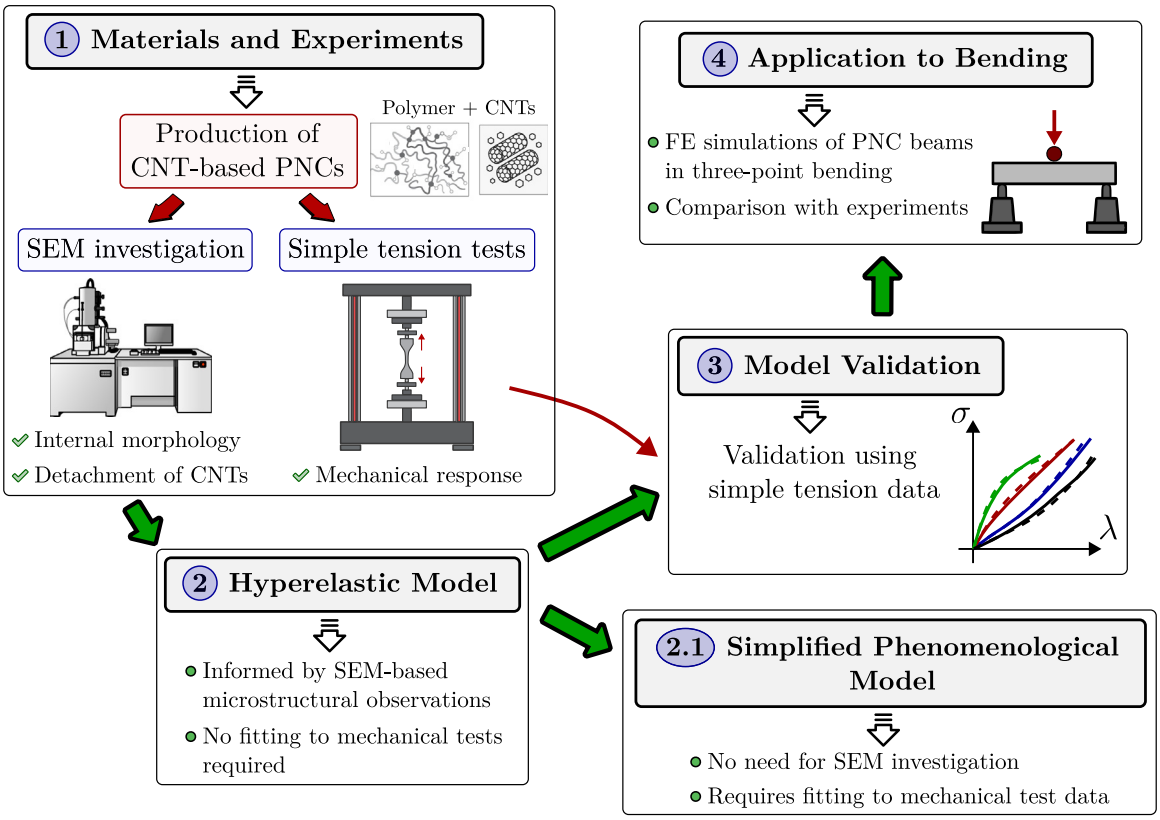

Fig. 1. Schematic representation of the research framework. (1) PNCs are produced by mixing a polymer matrix with multi-walled CNTs. The samples are analyzed through SEM imaging to investigate internal morphology and are subjected to simple tension tests to assess the mechanical response. (2) A hyperelastic model for CNT-based PNCs under large strains is proposed. The model is informed by microscopic observations and establishes a link between microstructure and macroscopic mechanical response, providing a predictive formulation that does not require calibration against stress–strain data. (3) The model is validated using experimental data from simple tension tests. (4) It is then applied to PNC beams under three-point bending to demonstrate its effectiveness and broader applicability. (2.1) Finally, a simplified phenomenological version of the hyperelastic model is proposed. This version does not require SEM analysis and follows the classical approach of nonlinear elasticity, relying on parameter fitting to stress–strain data.

In addition to the above, we introduce a simplified phenomenological version of the model that does not require SEM imaging for calibration and relies solely on stress–strain data. The physical meaning of the model parameters allows for straightforward calibration. The versatility of this version is demonstrated by applying it to additional experimental datasets available in the literature.

The structure of the present research is illustrated in Fig. 1. The manuscript is organized as follows. Section 2 describes the materials and production of the PNCs analyzed in this study, followed by SEM investigations and simple tension tests. Section 3 introduces the continuum mechanical framework for PNCs. In Section 4, the proposed hyperelastic model is developed by incorporating insights gained from SEM analysis to establish a link between microscopic features and continuum-scale mechanical behavior. Section 5 presents the calibration of model parameters based on SEM observations and the resulting stress–strain predictions, validated against simple tension experiments. Section 6 demonstrates the application of the model to predict the response of PNC beams under three-point bending. The model is implemented in the FE software COMSOL Multiphysics, where the hyperelastic PNC is modeled using a user-defined SEF within a 2D plane stress framework. The simulation results are compared with experimental data from bending tests. Section 7 introduces a simplified phenomenological version of the model, which can be calibrated using only stress–strain data. This formulation is then applied to additional datasets available in the literature. Finally, conclusions are provided in Section 8.

2. Materials and experimental methods

This section outlines the materials and experimental procedures of this study. First, the preparation of PNC samples is described, including the incorporation of multi-walled CNTs into the polymer matrix. Subsequently, the microscopy analyses conducted to investigate the morphology and dispersion of CNTs are presented. Finally, the methodology for the simple tension tests performed on the prepared samples is outlined.

2.1. Sample preparation

Polymer nanocomposites were prepared by mixing a rubber silicone matrix with multi-walled CNTs. The rubber matrix consisted of liquid silicone rubber supplied by RESIN PRO. This silicone rubber has a density $\rho_m = 1.1$ g/cm^3 and is provided in two components A and B, which were mixed at a 1:1 ratio. The working time of the rubber compound is approximately 1 h at 20 °C, with complete polymerization achieved after 24 h. The CNTs used as nanofiller reinforcement were supplied by Nanografi Nano Technology. According to the manufacturer, they have a reported purity exceeding 96% and a density $\rho_n = 2$ g/cm^3.

We first weighed the CNTs and components A and B of the silicone matrix using an analytical balance KERN ADB-200-4 with a readability of 0.1 mg. The CNTs were then added exclusively to component A to facilitate proper mixing. This solution was mechanically stirred for 15 min at 600 rpm using a mechanical stirrer AM 20-D ARGOlab to

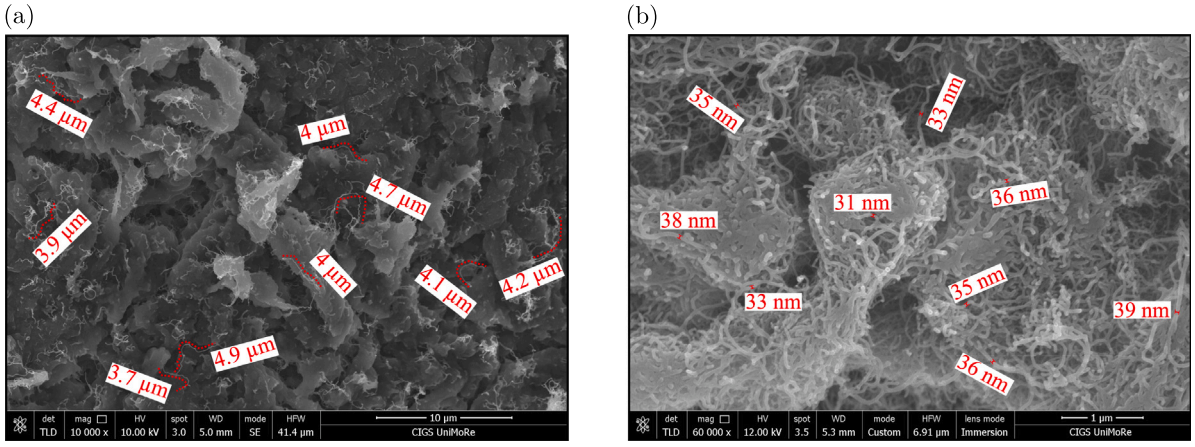

Fig. 2. SEM images of bulk multi-walled CNTs prior to dispersion in the polymer matrix. (a) Image at 10000x magnification, showing the tendency of nanotubes to interact and form agglomerates. Isolated CNTs are highlighted with dotted red lines, and their lengths are measured, yielding an average length of approximately $l = 4.2$ µm. (b) Image at 60000x magnification, revealing predominantly agglomerated nanotubes, with individual diameters measured and reported. The average diameter is determined to be $d = 35$ nm. Based on these measurements, the aspect ratio of the CNTs is calculated as $s = l/d \approx 120$.

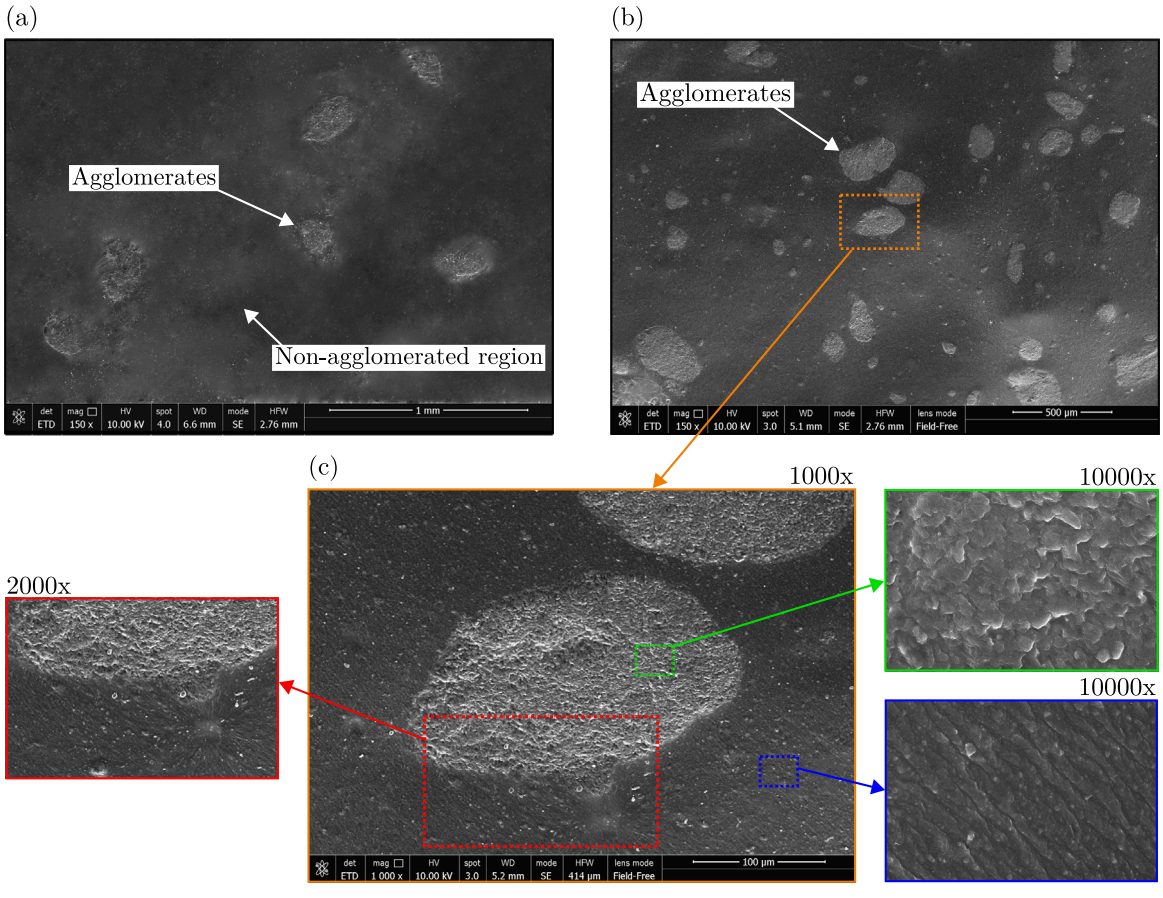

Fig. 3. SEM images of fractured PNC samples showing the internal structure and CNT dispersion within the polymer matrix. The images highlight the formation of agglomerates, which are regions with a higher concentration of CNTs. Figures (a) and (b) correspond to samples with 1 phr and 2.5 phr CNT content, respectively, while (c) presents a magnified view of an agglomerated region. From (a) and (b), it is observed that the agglomerate content increases with increasing CNT concentration in the samples.

ensure homogeneous dispersion of the CNTs, while avoiding any premature polymerization that could harden the solution. Subsequently, component B was added to the mixture and stirred for an additional 5 min.

The final mixture was cast into dog-bone-shaped molds to produce specimens for simple tension tests, as well as into other containers to obtain samples for microscopy analysis. The resulting PNCs contained CNTs at concentrations of 0.5, 1, 1.5, 2, and 2.5 phr, corresponding to volume fractions of 0.274%, 0.547%, 0.818%, 1.09%, and 1.36% of the nanocomposite, respectively.[1]

2.2. SEM investigation

Microscopy observations were conducted using an SEM FEI Nova NanoSEM 450 at the CIGS laboratories of the University of Modena and Reggio Emilia. The analysis was performed in two stages. First, the bulk multi-walled CNTs were examined to characterize their morphology and assess their initial state. Subsequently, the prepared PNC samples were analyzed to investigate their internal structure, focusing on the dispersion of CNTs and their interaction with the polymer matrix. The microscopy images in Fig. 2 demonstrate that the CNTs have an average diameter $d = 35$ nm and an average length $l = 4.2$ μm, corresponding to an aspect ratio of approximately $s = l/d \approx 120$. In their bulk state, the CNTs exhibit a strong tendency to form agglomerations due to their high aspect ratio and weak interactions. Furthermore, the CNTs are not straight but display a characteristic wavy morphology.

To investigate the dispersion and morphology of CNTs in the PNC samples, the specimens were first immersed in liquid nitrogen and subsequently fractured to expose their internal structure. The fractured surfaces were then examined using SEM to assess the distribution of CNTs within the polymer matrix. The resulting images are presented in Fig. 3.

Figs. 3(a) and (b) present SEM images of samples containing 1 and 2.5 phr of CNTs, respectively. We observe the tendency of CNTs to form agglomerates, namely localized regions with a higher concentration of nanotubes compared to the overall volume fraction in the material. In these images, the agglomerates appear as densely packed regions of CNTs, whereas the surrounding polymer matrix exhibits a lower nanotube concentration. Furthermore, a comparison between the two samples reveals that agglomeration is less pronounced at 1 phr, while at 2.5 phr, there is a significant increase in the presence of agglomerates. This suggests that as the CNT content increases, the likelihood of agglomeration becomes more prominent. Observations across multiple regions of the specimens, beyond the images presented here, indicate that the agglomerates are randomly distributed throughout the material. This randomness in distribution is consistent across the entire specimen.

Fig. 3(c) provides a magnified view of a representative agglomerate. The image distinctly highlights the agglomerate boundaries, showing a high concentration of CNTs within the agglomerate and a significantly lower density in the surrounding matrix. The zoomed-in images, outlined in green and blue, correspond to a magnification of 10000x, revealing the densely packed CNTs inside the agglomerate, while the surrounding polymer matrix exhibits a more dispersed nanotube distribution.

The high-magnification images in Fig. 3(c) show that the nanotubes are randomly oriented and retain their inherent waviness, consistent with observations made in the bulk material. The distribution of CNTs, both inside and outside the agglomerates, appears homogeneous, indicating that the sample fabrication and mixing process was effective.

[1] The conversion from nanofiller content in phr to volume fraction is given by $\phi_f = x_{\text{phr}}\rho_m / \left(100\rho_n + x_{\text{phr}}\rho_m\right)$, where x_{phr} is the nanofiller content expressed in phr, ρ_m is the matrix density, and ρ_n is the nanofiller density.

Note that the formation of agglomerates has also been reported by other authors (see, e.g., Ma et al., 2010; Rubel et al., 2019; Pan and Bian, 2019; Zeinedini and Shokrieh, 2024; Patti et al., 2016). This behavior is attributed to the high aspect ratio and large specific surface area of CNTs, which lead to strong inter-tube van der Waals interactions, making them prone to agglomeration in PNCs. This issue has been widely discussed in the literature, with various production methods proposed to reduce the presence of agglomerates. However, avoiding their formation remains an unresolved challenge.

The final SEM analysis was conducted to investigate the conditions under which CNTs detach from the polymer matrix. This information will be fundamental for the subsequent development of the hyperelastic model for PNCs. To examine this phenomenon, small PNC beams were precisely cut and subjected to tensile loading using a custom-built system, as shown in Fig. 4.

The system clamps the ends of two PNC specimens, applying and maintaining a controlled tensile stretch. The stretched specimens are then placed in the SEM chamber to be examined in their deformed state. This analysis was conducted on samples with a CNT content of 2.5 phr to ensure a high concentration of nanotubes, thereby enhancing the likelihood of observing potential detachment. One specimen was stretched to a final-to-initial length ratio of $\lambda = 2$, while the other was stretched to $\lambda = 2.5$.

The SEM images presented in Fig. 4 reveal that CNT detachment is predominantly concentrated within agglomerates, as the higher density of CNTs creates defects, making these regions more susceptible to failure and separation from the polymer matrix. Fig. 4(b) shows the condition of an agglomerate in the specimen stretched to a ratio of 2. A distinct rupture is observed, forming a cavity where the material has fractured. Even more extensive detachment is observed in the agglomerates of the specimen stretched to 2.5, as shown in Fig. 4(c). Here, a significant rupture occurs near the boundary of the agglomerate, leading to its substantial separation from the surrounding matrix. This indicates that as the applied stretch increases, the agglomerates become progressively more prone to detachment.

A magnified view of a detached agglomerate is provided in Fig. 4(d). The image clearly shows individual CNTs at the edges of the rupture, partially detached and suspended within the void. These observations provide direct evidence of CNT debonding under mechanical loading, highlighting the role of agglomeration in weakening the interfacial adhesion between CNTs and the polymer matrix.

In the specimen stretched to $\lambda = 2.5$, additional high-magnification SEM analysis was performed in regions outside the agglomerates, as shown in Fig. 4(e). The image clearly shows that the CNTs have aligned along the stretching direction, and no significant detachment is observed at this stage. Only slightly darker regions appear adjacent to certain CNTs, possibly indicating the very early onset of CNT-matrix separation. This suggests that, with continued stretching, detachment would likely develop in this region as well. Nonetheless, this could not be directly observed, as the specimen fails before reaching the stretch levels at which significant detachment is expected to occur.

In conclusion, the SEM analysis of CNT detachment led to the following observations:

- Detachment is predominantly concentrated within agglomerated regions, becoming evident at a stretch ratio of $\lambda = 2$, and significantly more pronounced at $\lambda = 2.5$, where extensive separation is observed.
- In non-agglomerated regions, at $\lambda = 2.5$, full alignment of CNTs along the stretching direction is observed, with no apparent signs of CNT-matrix detachment.

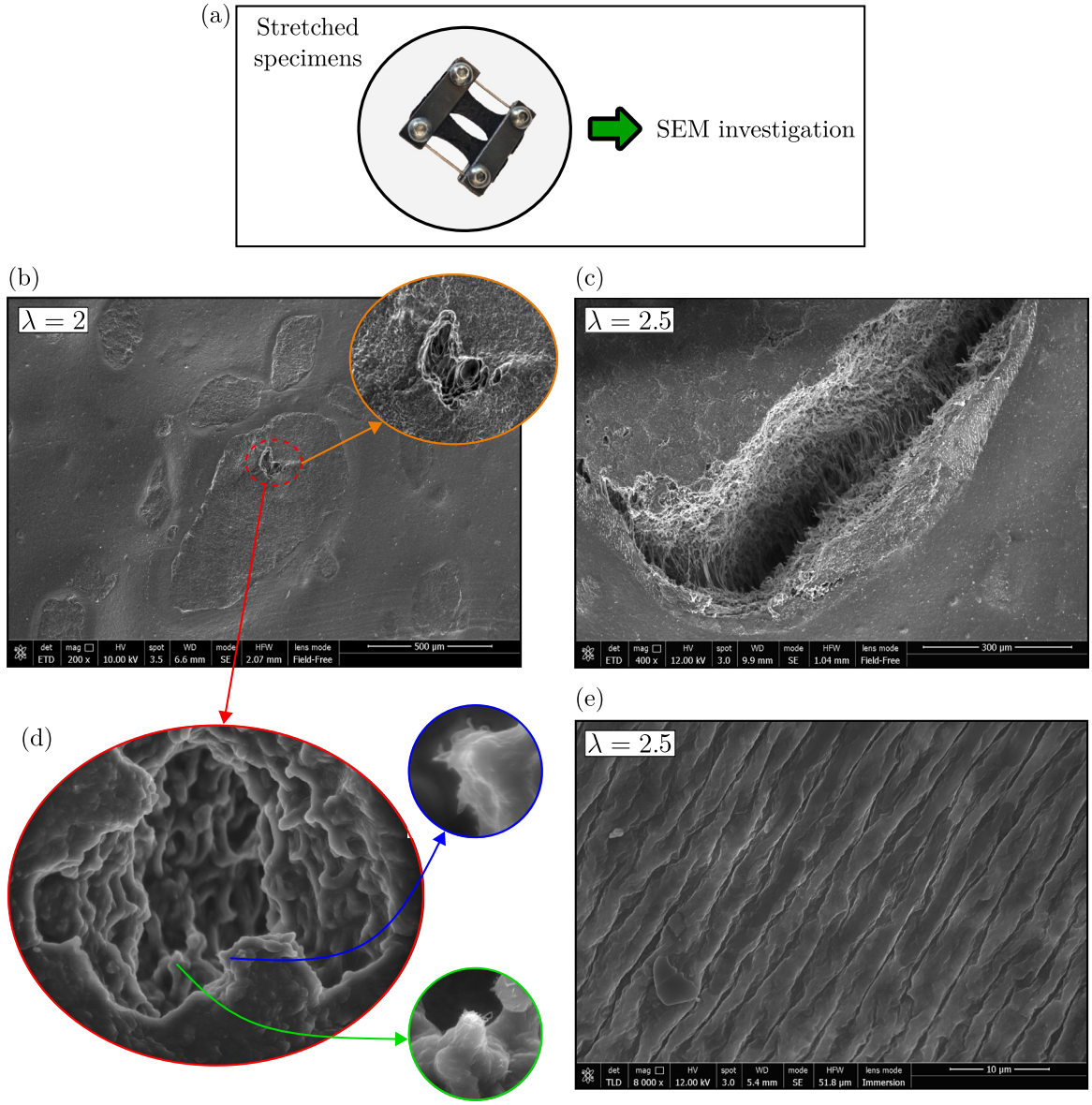

Fig. 4. SEM images of PNC samples in the stretched configuration, analyzed to investigate the detachment of CNTs from the polymer matrix. (a) Custom-built system used to stretch two specimens with a CNT content of 2.5 phr, maintained at stretch ratios λ of 2 and 2.5. (b) Initial signs of detachment within agglomerates at a stretch ratio of 2, with clear evidence of rupture. (c) Extensive detachment observed in the specimen stretched to 2.5, where the agglomerate visibly separates near its boundary with the surrounding matrix. (d) High-magnification view of the detached region, showing a cavity formed within the agglomerate. Further zoomed-in images reveal individual nanotubes that have separated. (e) Magnified view of a region outside an agglomerate at $\lambda = 2.5$, where full alignment of CNTs along the stretching direction is observed, with no apparent signs of CNT-matrix detachment.

2.3. Simple tension tests

The dog-bone specimens used for testing had an effective length of 60 mm, a height of 7 mm, and a thickness of 2.5 mm. For each PNC with varying CNT contents, three specimens were subjected to tensile testing until failure. Tests were also performed on specimens made solely of the silicone matrix.

The experiments were conducted using an Instron 5567 testing machine equipped with a 100 N load cell. A constant displacement rate of 120 mm/min was applied, corresponding to a strain rate of 0.033 s^{-1}, which is commonly classified as quasi-static (see, for example, Meunier et al., 2008; Tomita et al., 2008; Cheng and Chen, 2003). To capture the test process, a Panasonic LUMIX DC-GH6 camera was positioned orthogonally to the specimen to record videos. The captured footage was later processed using digital image correlation (DIC) with the *Ncorr* MATLAB package. Further details on this process can be found in Pelliciari et al. (2023, 2025).

Using the DIC analysis, we determined the longitudinal and lateral stretches, λ_x and λ_y. The nominal stress, σ_x, was calculated as $\sigma_x = F/A$, where F represents the applied force measured by the testing machine, and A is the initial cross-sectional area of the specimen. For each PNC composition, the results across three specimens exhibited minimal variation. Therefore, we considered the average stretches and stresses from the three tests.

The experimental data on lateral vs. longitudinal stretches indicated that both the pure matrix and the PNCs with varying CNT contents exhibit near-incompressibility, with negligible volumetric deformations.

This behavior was expected, as the polymer matrix itself is nearly incompressible, and the addition of small amounts of nanoparticles does not significantly alter this characteristic.

3. Continuum mechanics framework

In this section, we introduce the fundamental continuum mechanics framework for CNT-based PNCs, which are modeled within the framework of hyperelasticity. We provide a summary of finite deformation kinematics, governing equations, and modeling assumptions.

3.1. Kinematics

The PNC is modeled as a continuous body with a stress-free reference configuration. The deformation of the body is described by the deformation gradient $\mathbf{F} = \partial \boldsymbol{x}/\partial \boldsymbol{X}$, where $\boldsymbol{X}$ represents the position of a material point in the reference configuration, and $\boldsymbol{x}$ denotes its position in the deformed configuration. The local volume ratio is given by $J = \det \mathbf{F} > 0$. The right and left Cauchy–Green deformation tensors are defined as $\mathbf{C} = \mathbf{F}^T\mathbf{F}$ and $\mathbf{B} = \mathbf{F}\mathbf{F}^T$, respectively (Ogden, 1997; Pelliciari and Tarantino, 2022).

We consider the multiplicative decomposition of the deformation gradient $\mathbf{F}$ as follows (Flory, 1961; Ogden, 1978; Sansour, 2008):

$$\mathbf{F} = \left(J^{1/3}\mathbf{I}\right)\bar{\mathbf{F}}, \tag{1}$$

where $\mathbf{F}$ is decomposed into a volumetric part, $J^{1/3}\mathbf{I}$, and an isochoric part, $\bar{\mathbf{F}}$, satisfying the constraint $\det \bar{\mathbf{F}} = 1$. Symbol $\mathbf{I}$ denotes the second-order identity tensor. The modified counterparts of the right Cauchy–Green tensor $\mathbf{C}$ and the left Cauchy–Green tensor $\mathbf{B}$, associated with $\bar{\mathbf{F}}$, are denoted as $\bar{\mathbf{C}}$ and $\bar{\mathbf{B}}$, respectively. Using (1) we write

$$\begin{aligned} &\mathbf{C} = \mathbf{F}^T\mathbf{F} = J^{2/3}\bar{\mathbf{C}}, \qquad \bar{\mathbf{C}} = \bar{\mathbf{F}}^T\bar{\mathbf{F}}, \\ &\mathbf{B} = \mathbf{F}\mathbf{F}^T = J^{2/3}\bar{\mathbf{B}}, \qquad \bar{\mathbf{B}} = \bar{\mathbf{F}}\bar{\mathbf{F}}^T. \end{aligned} \tag{2}$$

The CNTs embedded in the continuum are modeled as fibers with a mean initial orientation defined by the referential unit vector $\boldsymbol{a}_0$, satisfying $|\boldsymbol{a}_0| = 1$. Under deformation, the fibers are mapped into their current configuration, where their mean spatial orientation is given by $\boldsymbol{a} = \mathbf{F}\boldsymbol{a}_0$, and the stretch along the mean direction of fibers is $|\boldsymbol{a}|$.

3.2. Hyperelasticity for PNCs

We adopt the standard approach of additive decomposition of the SEF, which is physically justified given the low to moderate volume fraction of CNTs embedded in the elastomer matrix (Cantournet et al., 2007). The total SEF, W, is expressed as the sum of contributions from different phases of the nanocomposite: the pure elastomer matrix, the non-agglomerated CNT regions, and the agglomerated CNT regions (Fig. 5).

These phases are treated separately to account for their distinct mechanical behaviors. The elastomer matrix is modeled using isotropic hyperelasticity, while the contributions from CNTs and their agglomerates are described within the framework of anisotropic hyperelasticity.

The SEF contributions are defined as follows: W_m for the elastomer matrix, W_n for the CNTs in non-agglomerated regions, and W_a for the CNTs in agglomerated regions. Agglomerates have a higher CNT concentration and, consequently, different elastic properties compared to the surrounding material. Using a rule-of-mixtures approach (Shi et al., 2004), we define the SEFs within the *inside* and *outside* regions of the agglomerates as:

$$\begin{aligned} W_{\text{in}} &= (1-\phi_a)W_m + \phi_a W_a, \\ W_{\text{out}} &= (1-\phi_m)W_m + \phi_m W_n, \end{aligned} \tag{3}$$

where ϕ_a is the volume fraction of CNTs inside the agglomerates, and ϕ_m is the volume fraction of CNTs outside the agglomerates. The parameter ϕ_m is calculated as

$$\phi_m = \frac{\phi_f - \xi\phi_a}{1-\xi}, \tag{4}$$

with ϕ_f denoting the total volume fraction of CNTs, and ξ being the proportion of the total volume occupied by the agglomerated regions.[2] By summing the contributions from the inside and outside regions, the total SEF of the nanocomposite is expressed as

$$W = (1-\xi)W_{\text{out}} + \xi W_{\text{in}} = (1-\phi_f)W_m + (\phi_f - \xi\phi_a)W_n + \xi\phi_a W_a. \tag{5}$$

The contribution of the isotropic matrix is generally formulated for compressible materials and is therefore expressed using an isochoric-volumetric split as $W_m = W_d(\bar{\mathbf{C}}) + W_h(J)$. In contrast, the anisotropic contributions from nanotubes in non-agglomerated and agglomerated regions are given as $W_n = W_n(\mathbf{C}, \boldsymbol{a}_0)$ and $W_a = W_a(\mathbf{C}, \boldsymbol{a}_0)$, respectively.[3] Note that the isochoric-volumetric split is not applied to the anisotropic part, as doing so would lead to unphysical stress responses (see, e.g., Sansour, 2008; Gültekin et al., 2019; Teichtmeister and Holzapfel, 2022; Holzapfel and Ogden, 2020a).

The representation theory of scalar-valued tensor functions for anisotropic materials with a single fiber family establishes that the SEF depends on five invariants (Spencer, 1984; Zheng, 1994; Cai et al., 2016; Yavari and Goriely, 2021). Specifically, the isotropic contribution W_m depends on two isochoric invariants in addition to the volume ratio, which are given by

$$\bar{I}_1 = \operatorname{tr}\bar{\mathbf{C}}, \quad \bar{I}_2 = \operatorname{tr}\left(\operatorname{cof}\bar{\mathbf{C}}\right), \quad I_3 = \det\mathbf{C} = J^2, \tag{6}$$

where the cofactor of the tensor $\bar{\mathbf{C}}$ is expressed as $\operatorname{cof}\bar{\mathbf{C}} = \bar{\mathbf{C}}^{-T}\det\bar{\mathbf{C}}$. On the other hand, the anisotropic contributions W_n and W_a depend on two additional mixed invariants (Guo et al., 2006):

$$I_4 = \mathbf{C} : \mathbf{H}, \quad I_5 = \mathbf{C}^2 : \mathbf{H}, \tag{7}$$

where the generalized structure tensor (GST) $\mathbf{H}$ is a symmetric tensor that was introduced by Gasser et al. (2006) to represent general fiber orientation dispersions in a continuum framework.

Gasser et al. derived an analytical expression for the structure tensor corresponding to a general transversely isotropic fiber distribution, which encompasses as limiting cases an isotropic (random) fiber distribution and a fully aligned fiber distribution. In this work, we focus on these two limiting cases, with particular emphasis on the isotropic distribution, since the nanoscale dimensions of CNTs make preferential alignment difficult to achieve in practice. Indeed, CNTs are typically randomly distributed in most technologically manufactured PNCs, although some studies have demonstrated the fabrication of PNCs with aligned CNTs (Marconnet et al., 2011; Khan et al., 2013). This scenario is also addressed by the GST formulation discussed above.[4]

The formulation proposed by Gasser et al. is based on an orientation density function, which statistically characterizes fiber alignment. In Gasser et al. (2006), the following compact form of the GST was derived:

$$\mathbf{H} = \kappa\mathbf{I} + (1-3\kappa)\boldsymbol{a}_0 \otimes \boldsymbol{a}_0, \tag{8}$$

where $\otimes$ denotes the tensor product and $\kappa \in [0, 1/3]$ is the dispersion parameter, representing fiber distribution in an integral sense. The limiting cases are as follows:

[2] Parameters ξ and ϕ_a, representing the volume fraction occupied by agglomerates and the volume content of CNTs within the agglomerates, respectively, will be estimated using SEM images. The volume content of CNTs in the matrix, ϕ_m, is subsequently computed using (4), ensuring that all parameters describing the internal morphology are determined.

[3] We assume that the mean orientation $\boldsymbol{a}_0$ of the CNTs is the same in both agglomerated and non-agglomerated regions; that is, CNTs retain their orientation distribution inside as well as outside the agglomerates.

[4] For more general orientation distributions that extend beyond the transversely isotropic case and the scope of this paper, the reader is referred to Cortes and Elliott (2014), Gizzi et al. (2018). Note that such cases require numerical solutions, as closed-form results are generally not available.

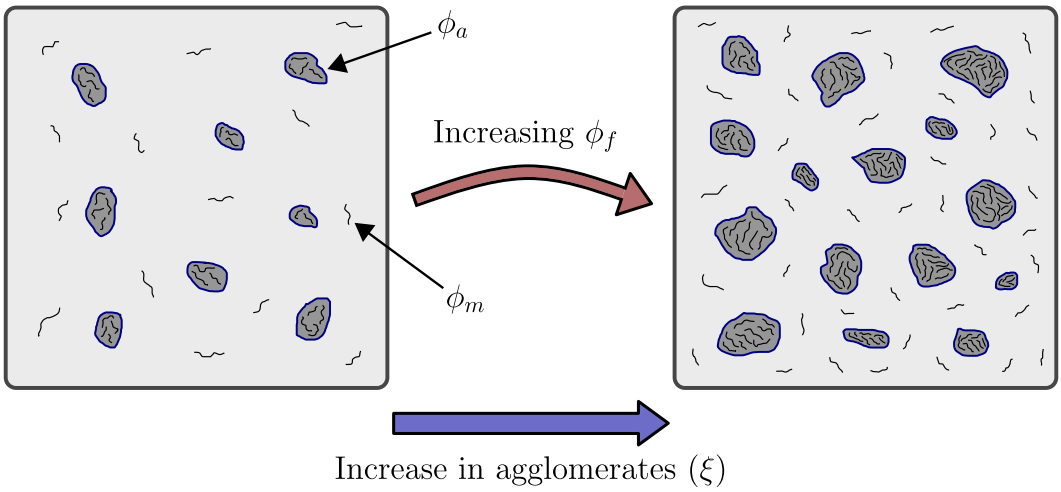

Fig. 5. Schematic representation of the internal morphology of the PNC, illustrating the increase in agglomerated regions as the overall CNT volume fraction ϕ_f increases. The volume fraction of the agglomerates is denoted by ξ. Agglomerated regions contain a higher CNT concentration, represented by ϕ_a, while non-agglomerated regions have a lower CNT content, denoted as ϕ_m. The model thus considers three distinct phases: the matrix, CNTs in agglomerated regions, and CNTs in non-agglomerated regions.

- For perfectly aligned fibers ($\kappa = 0$), the GST reduces to $\mathbf{H} = \boldsymbol{a}_0 \otimes \boldsymbol{a}_0$, and the invariant I_4 simplifies to the squared stretch in the fiber direction, i.e., $I_4 = \lambda^2(\boldsymbol{a}_0)$.
- For an isotropic fiber distribution ($\kappa = 1/3$), the GST simplifies to $\mathbf{H} = (1/3)\mathbf{I}$, leading to $I_4 = I_1/3$.

Based on the physical nature of CNTs as high-aspect-ratio fibers, and following well-established approaches for fiber-reinforced hyperelastic materials (Holzapfel and Ogden, 2025), we consider only the invariant I_4 in describing the CNT contributions. This leads to the simplified dependencies

$$W_m = W_m(\bar{I}_1, \bar{I}_2, I_3), \quad W_n = W_n(I_4), \quad W_a = W_a(I_4). \tag{9}$$

Compressive fibers are typically assumed not to contribute to the overall mechanical response. This issue is addressed by nullifying the anisotropic part of $\mathbf{H}$ when the stretch in the main fiber direction is compressive (Holzapfel and Ogden, 2010; Melnik et al., 2015; Peng et al., 2005; Pandolfi and Vasta, 2012). In this case, the structure tensor is defined as:

$$\mathbf{H} = \begin{cases} \kappa\mathbf{I} + (1-3\kappa)\boldsymbol{a}_0 \otimes \boldsymbol{a}_0, & \boldsymbol{a}_0 \otimes \boldsymbol{a}_0 : \mathbf{C} \geq 1, \\ \kappa\mathbf{I}, & \boldsymbol{a}_0 \otimes \boldsymbol{a}_0 : \mathbf{C} < 1. \end{cases} \tag{10}$$

An alternative scheme for excluding the contribution of compressed fibers, referred to as the iGST approach, was proposed by Melnik et al. (2015), and may be considered as an alternative to the formulation above.

Remark 1. The dispersion parameter κ may formally take values in the range $(1/3, 1/2]$, with $\kappa = 1/2$ corresponding to the case of complete alignment in the plane perpendicular to the mean fiber direction $\boldsymbol{a}_0$. However, the original formulation by Gasser et al. was based on a transversely isotropic and π-periodic von Mises distribution, which restricts κ to the interval $[0, 1/3]$ (see Remark 4.1 and Fig. 3 in Gasser et al. (2006)). In the case of more general fiber distributions that yield $\kappa > 1/3$, the standard GST formulation in (10) may result in unphysical mechanical responses, such as negative stress under tensile strain. To address this, Melnik et al. (2015) proposed modified definitions of the GST that resolve these issues. For the purposes of the present study, however, the formulation in (10) remains appropriate.

3.3. Incompressibility assumption and stress response

As described in Section 2.3, experimental data on lateral and longitudinal stretches indicate that the analyzed PNCs exhibit near-incompressibility. Based on this observation, we assume that the material is incompressible from this point forward. For incompressible materials, the deformation is isochoric, meaning that $J = 1$. Consequently, the dependency of the isotropic contribution further reduces to $W_m = W_m(I_1, I_2)$.[5]

Given this assumption, the Cauchy stress tensor $\mathbf{T}$ is expressed as (Ogden, 1997):

$$\mathbf{T} = \frac{\partial W}{\partial \mathbf{F}}\mathbf{F}^T - p\mathbf{I}, \tag{11}$$

where p represents the arbitrary hydrostatic pressure associated with the incompressibility constraint. The contributions from the elastomer matrix, non-agglomerated regions, and agglomerated regions are separated as

$$\mathbf{T}_m = \frac{\partial W_m}{\partial \mathbf{F}}\mathbf{F}^T - p_m\mathbf{I}, \quad \mathbf{T}_n = \frac{\partial W_n}{\partial \mathbf{F}}\mathbf{F}^T - p_n\mathbf{I}, \quad \mathbf{T}_a = \frac{\partial W_a}{\partial \mathbf{F}}\mathbf{F}^T - p_a\mathbf{I}, \tag{12}$$

with $p = (1-\phi_f)p_m + (\phi_f - \xi\phi_a)p_n + \xi\phi_a p_a$. The standard results from the representation theorem (Truesdell and Noll, 2004), combined with the application of the chain rule for tensor derivatives, lead to the following expressions (Schröder et al., 2008):

$$\mathbf{T}_m = -p_m\mathbf{I} + 2\left(\frac{\partial W_m}{\partial I_1}\mathbf{B} - \frac{\partial W_m}{\partial I_2}\mathbf{B}^{-1}\right), \quad \mathbf{T}_n = -p_n\mathbf{I} + 2\frac{\partial W_n}{\partial I_4}\mathbf{B}\mathbf{H},$$
$$\mathbf{T}_a = -p_a\mathbf{I} + 2\frac{\partial W_a}{\partial I_4}\mathbf{B}\mathbf{H}. \tag{13}$$

The total Cauchy stress of the PNC is obtained additively as

$$\mathbf{T} = (1-\phi_f)\mathbf{T}_m + (\phi_f - \xi\phi_a)\mathbf{T}_n + \xi\phi_a\mathbf{T}_a. \tag{14}$$

[5] Under the incompressibility assumption, the isochoric strain invariants $\bar{I}_1$ and $\bar{I}_2$ reduce to the standard invariants $I_1 = \operatorname{tr}\mathbf{C}$ and $I_2 = \operatorname{tr}(\operatorname{cof}\mathbf{C})$. Accordingly, the strain energy is hereafter expressed as a function of I_1 and I_2.

The first Piola–Kirchhoff stress tensor is obtained from the Cauchy stress via the standard transformation $\mathbf{P} = \mathbf{T}\mathbf{F}^{-T}$, writing

$$\mathbf{P} = (1-\phi_f)\mathbf{P}_m + (\phi_f - \xi\phi_a)\mathbf{P}_n + \xi\phi_a\mathbf{P}_a, \tag{15}$$

where the individual contributions from the elastomer matrix, non-agglomerated regions, and agglomerated regions are given by

$$\mathbf{P}_m = \mathbf{T}_m\mathbf{F}^{-T}, \quad \mathbf{P}_n = \mathbf{T}_n\mathbf{F}^{-T}, \quad \mathbf{P}_a = \mathbf{T}_a\mathbf{F}^{-T}. \tag{16}$$

3.4. Orientation-dependent contribution of CNTs to Young's modulus

For the following developments, we consider the case of uniaxial extension with the stretch applied along the preferred mean fiber direction $\boldsymbol{a}_0$. We introduce a Cartesian coordinate system (x, y, z) and, without loss of generality, assume that $\boldsymbol{a}_0$ is aligned with the x-axis, i.e., $\boldsymbol{a}_0 = \boldsymbol{e}_x$.

Considering that the material is incompressible, the left and right Cauchy–Green deformation tensors are given by (Anssari-Benam and Bucchi, 2021):

$$\mathbf{B} = \mathbf{C} = \lambda_x^2\,\boldsymbol{e}_x\otimes\boldsymbol{e}_x + \frac{1}{\lambda_x}\left(\mathbf{I} - \boldsymbol{e}_x\otimes\boldsymbol{e}_x\right), \tag{17}$$

and the expression of invariant I_4 becomes $I_4 = \lambda_x^2 - 2\kappa(\lambda_x^3-1)/\lambda_x$. The Cauchy stress tensor associated with W_n from $(13)_2$ assumes the form:

$$\mathbf{T}_n = -p_n\mathbf{I} + 2\left[\lambda_x^2(1-2\kappa)\boldsymbol{e}_x\otimes\boldsymbol{e}_x + \frac{\kappa}{\lambda_x}\left(\mathbf{I} - \boldsymbol{e}_x\otimes\boldsymbol{e}_x\right)\right]\frac{\partial W_n}{\partial I_4}. \tag{18}$$

The fictitious pressure p_n is determined by enforcing the condition of vanishing normal stress in the directions orthogonal to $\boldsymbol{e}_x$, which yields $p_n = 2\lambda_x^{-1}\kappa\,\partial W_n/\partial I_4$. Substituting this into (18) provides the final expression for the Cauchy stress. The nominal stress–stretch relation is then obtained via the transformation given in $(16)_2$

$$\sigma_{x,n} = \frac{2}{\lambda_x^2}\left[\lambda_x^3(1-2\kappa) - \kappa\right]\frac{\partial W_n}{\partial I_4}. \tag{19}$$

It is clear from (19) that the condition of a stress-free reference configuration for perfectly aligned fibers in the x direction ($\kappa = 0$) requires $\partial W_n/\partial I_4\big|_{I_4=1} = 0$. The same condition must also hold for any other value of κ, except in the case of a randomly oriented (isotropic) distribution. In that case, with $\kappa = 1/3$, the stress component $\sigma_{x,n}$ vanishes in the reference configuration even if the strain energy function satisfies $\partial W_n/\partial I_4\big|_{I_4=1} \neq 0$. This is physically due to the fact that, in an isotropic distribution in the reference configuration, the initial stresses in the fibers balance each other out. We elaborate further on this in the following developments.

By differentiating (19) with respect to λ_x, we obtain the tangent modulus associated with the uniaxial response:

$$\frac{\partial\sigma_{x,n}}{\partial\lambda_x} = \frac{4}{\lambda_x^4}\frac{\partial^2 W_n}{\partial I_4^2}\left[(2\kappa-1)\lambda_x^3 + \kappa\right]^2 + \frac{2}{\lambda_x^3}\frac{\partial W_n}{\partial I_4}\left[\lambda_x^3 - 2\kappa\left(\lambda_x^3 - 1\right)\right]. \tag{20}$$

Assuming that the strain energy function satisfies $\partial W_n/\partial I_4\big|_{I_4=1} = 0$, and evaluating the expression in the reference configuration, the second term vanishes. The contribution of CNTs to the Young's modulus then simplifies to

$$E_n = \left.\frac{\partial\sigma_{x,n}}{\partial\lambda_x}\right|_{\lambda_x=1} = 4\,(1-3\kappa)^2\left.\frac{\partial^2 W_n}{\partial I_4^2}\right|_{I_4=1}. \tag{21}$$

The two limiting cases of fully aligned and randomly oriented CNTs yield the following results:

$$\begin{cases} E_n = 4\left.\dfrac{\partial^2 W_n}{\partial I_4^2}\right|_{I_4=1}, & \kappa = 0 \text{ (aligned)}, \\ E_n = 0, & \kappa = 1/3 \text{ (random isotropic)}. \end{cases} \tag{22}$$

This highlights that, for an isotropic (random) distribution of nanofibers, the contribution to the elastic modulus of the PNC vanishes if the strain energy function W_n satisfies $\partial W_n/\partial I_4\big|_{I_4=1} = 0$. In such a case, the fibers would not contribute to the initial stiffness of the material. However, this result is not consistent with experimental evidence. Tests on specimens with isotropically distributed CNTs clearly demonstrate a measurable increase in the elastic modulus compared to the neat matrix.[6] On the other hand, if a SEF is considered such that $\partial W_n/\partial I_4\big|_{I_4=1} \neq 0$, then for the case $\kappa = 1/3$ relation (20) yields

$$E_n = \left.\frac{\partial\sigma_{x,n}}{\partial\lambda_x}\right|_{\lambda_x=1} = 2\left.\frac{\partial W_n}{\partial I_4}\right|_{I_4=1}. \tag{23}$$

The above discussion leads to the following conclusion. When using the GST approach as introduced in Gasser et al. (2006) to account for the orientation of CNTs, it appears not to be possible to define a single strain energy function W_n that simultaneously satisfies both of the following conditions: (1) the reference configuration is stress-free in the case of aligned CNTs, and (2) randomly oriented CNTs contribute to an increase in the Young's modulus of the nanocomposite. In light of this, applying the GST framework across different orientation states in CNT-reinforced nanocomposites requires particular care. In the isotropic limit, the energy function should allow for a nonzero initial stiffness contribution.

In this work, we focus on randomly oriented CNTs and therefore consider only the case $\kappa = 1/3$ from this point onward. To capture the experimentally observed increase in initial stiffness, we adopt a strain energy function that satisfies the condition $\partial W_n/\partial I_4\big|_{I_4=1} \neq 0$.

Note that all of the above results were derived considering the contribution of CNTs in the non-agglomerated regions (W_n). However, the same expressions apply to the agglomerated regions by replacing W_n with W_a. In this case, the corresponding stress and Young's modulus are denoted by $\sigma_{x,a}$ and E_a, respectively.

4. Proposed hyperelastic formulation for randomly oriented CNT-based PNCs

This section presents the hyperelastic model developed to describe randomly oriented (isotropic) CNT-reinforced PNCs. The insights gained from the SEM analyses, which revealed the internal morphology of the material, are used to establish connections between the microstructural features and the macroscopic mechanical response. A multi-scale approach is thus employed to bridge the microscopic characteristics with the continuum-level modeling, in the framework of hyperelasticity.

4.1. Growth of agglomerated regions

From the SEM investigation, we observed that the agglomerate content increases as the overall CNT volume fraction in the nanocomposite increases. This behavior of nanoparticles is commonly captured phenomenologically using sigmoidal growth models (Wang et al., 2014). We describe the growth of the volume content of agglomerations, ξ, as a function of ϕ_f using the Hill equation[7] (Gesztelyi et al., 2012):

$$\xi = \frac{1}{1 + \left(\phi_c/\phi_f\right)^2}, \tag{24}$$

where ϕ_c is the critical volume fraction at which half of the nanoparticles form agglomerates ($\xi = 0.5$ when $\phi_f = \phi_c$). The parameter ϕ_c lies within the range $(0, 1)$ and should be calibrated based on SEM images or other morphological observations, to ensure that the model reflects

[6] This is shown in Section 5 by our experimental data in simple tension and is also widely reported in the literature on mechanical testing of PNCs; see, for example, Qian et al. (2000), Fu et al. (2019), Cantournet et al. (2007), Papageorgiou et al. (2020).

[7] The Hill equation is a modified form of the logistic function, widely used to model systems that exhibit growth toward a saturation limit. It is commonly applied in fields such as pharmacology and materials science to describe nonlinear cooperative behavior.

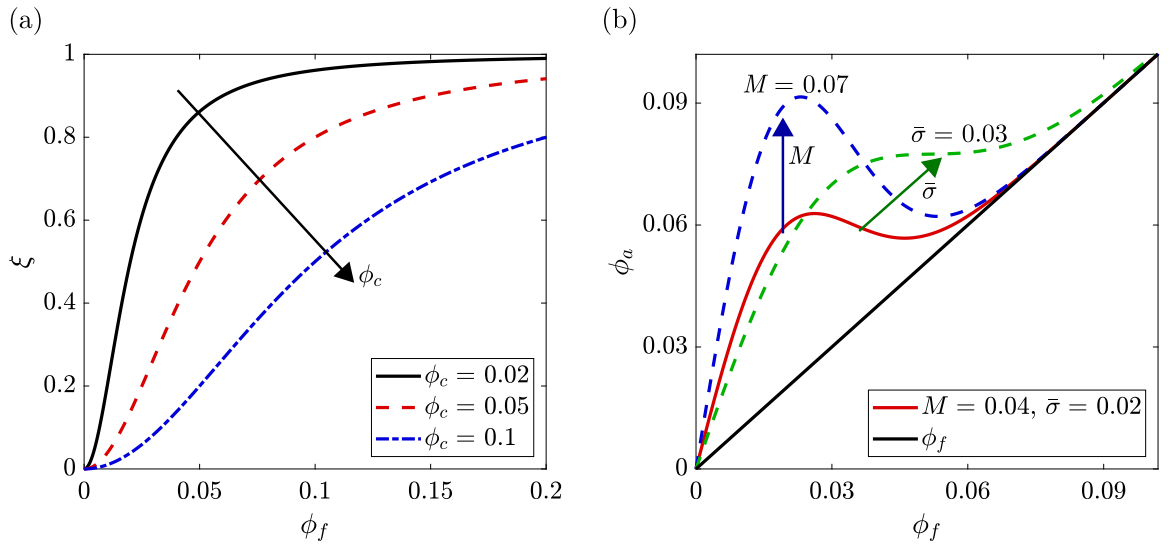

Fig. 6. Evolution of the agglomerate volume fraction ξ and the CNT content within agglomerates ϕ_a as functions of the total CNT volume fraction ϕ_f. (a) Growth of the agglomerate phase ξ, defined by (24), exhibiting a sigmoidal trend controlled by the critical volume fraction ϕ_c. (b) Evolution of the CNT content within agglomerates ϕ_a, defined by (28) based on a Rayleigh distribution, with parameters M and $\bar{\sigma}$ governing the peak magnitude and the distribution width, respectively.

the experimentally observed agglomeration behavior. Fig. 6(a) shows the function ξ, highlighting the general trend and the effect of varying ϕ_c.

This sigmoidal model[8] describes the stages of the agglomeration process in nanocomposites:

(1) At low filler contents, the probability of nanoparticles encountering each other is low, resulting in sparse interactions and slow agglomerate formation.
(2) As the volume fraction approaches the critical threshold ϕ_c, interactions between nanoparticles become more frequent, leading to accelerated agglomeration.
(3) At higher filler contents, the process reaches a plateau as available space and bonding sites become exhausted.

4.2. CNT content in agglomerates

The variation in CNT content between agglomerated and non-agglomerated regions introduces spatial heterogeneity within the composite. This phenomenon is modeled statistically using a Weibull distribution, a commonly employed approach for capturing variability in material properties (Mahmoodi and Khamehchi, 2024; Genet et al., 2014). The probability density function of the Weibull distribution is given by (Liu et al., 2025):

$$f(x) = \begin{cases} \frac{m}{\eta}\left(\frac{x}{\eta}\right)^{m-1} e^{-(x/\eta)^m}, & x > 0, \\ 0, & x \le 0, \end{cases} \tag{25}$$

where $m > 0$ is the shape parameter and $\eta > 0$ is the scale parameter.

For $m = 2$ and $\eta = \sqrt{2}\bar{\sigma}$, where $\bar{\sigma}$ is a scale parameter that controls the width of the distribution, the Weibull distribution simplifies to the Rayleigh distribution

$$f(x) = \frac{x}{\bar{\sigma}^2} e^{-x^2/(2\bar{\sigma}^2)}, \tag{26}$$

which is used to model nonnegative-valued quantities, making it suitable for our application. The Rayleigh distribution reaches its maximum value $1/(\bar{\sigma}\sqrt{e})$ at $x = \bar{\sigma}$. For convenience and to adapt the Rayleigh distribution to our specific modeling needs, we introduce a normalization factor to ensure that the maximum value of the function equals a desired value M:

$$f(x) = \frac{M\sqrt{e}}{\bar{\sigma}} x\, e^{-x^2/(2\bar{\sigma}^2)}. \tag{27}$$

The above normalization allows for the direct specification of the peak value, which is useful in this context since the maximum of the distribution holds a well-defined physical significance, as will become clear later.

The statistical function in (27) is used in this work to describe the evolution of the content ϕ_a of CNTs within the agglomerates as a function of the overall content ϕ_f. However, there are two physical constraints that must be considered:

(1) The CNT fraction within the agglomerates must always be greater than or equal to the overall CNT fraction in the PNC, ensuring that $\phi_a \ge \phi_f$.
(2) The fraction of CNTs within the agglomerates cannot exceed the total CNT content in the PNC, meaning $\xi\phi_a \le \phi_f$.

To satisfy the first condition, we consider (27) and propose the following modified form:

$$\phi_a = \phi_f \left[1 + \frac{M\sqrt{e}}{\bar{\sigma}} e^{-\phi_f^2/(2\bar{\sigma}^2)}\right]. \tag{28}$$

This ensures that $\phi_a \ge \phi_f$ for all values of ϕ_f. We can now express the second condition as follows:

$$M \le \frac{\bar{\sigma}\phi_c^2}{\sqrt{e}\,\phi_f^2} e^{\phi_f^2/(2\bar{\sigma}^2)}, \quad \text{for all } \phi_f \in (0,1). \tag{29}$$

The minimum of the right-hand side of (29) is found by imposing stationarity, which occurs at $\phi_f = \sqrt{2}\,\bar{\sigma}$. Substituting this value back

[8] Empirical evidence supports the use of sigmoidal functions in modeling nanoparticle behavior in composites and similar systems where nonlinear scaling occurs (Rubel et al., 2019; Pan and Bian, 2019). A related framework is the percolation theory (Azimi and Sharifzadeh, 2025; Starr et al., 2003), which describes the transition from isolated particles to the formation of a connected network as a critical volume fraction is exceeded. Both approaches share the underlying concept of a critical threshold that marks a nonlinear shift in material behavior.

into the inequality yields the following constraint:

$$M \leq \frac{\sqrt{e}\,\phi_c^2}{2\bar{\sigma}}. \tag{30}$$

This constraint ensures that the modified Rayleigh function satisfies the physical conditions governing the distribution of CNTs within the agglomerates.

Fig. 6(b) shows the function ϕ_a and the influence of M and $\bar{\sigma}$ on its shape. The calibration of parameters M and $\bar{\sigma}$ in (28) is performed using data extracted from SEM images. When sufficient microscopy data is available, this process is straightforward, as M is connected to the maximum volume fraction of CNTs within agglomerates, while $\bar{\sigma}$ defines the width of the statistical distribution.

Remark 2. Since ϕ_a represents a volume fraction, it is physically required that $\phi_a \leq 1$. Although (28) suggests that ϕ_a could in principle exceed unity as $\phi_f \to 1$, such a scenario is unrealistic for PNCs, where typical filler contents are small (values as high as $\phi_f = 0.1$–0.2 are already very large). Furthermore, for the parameter values relevant to our study, ϕ_a tends asymptotically to ϕ_f as ϕ_f increases, as shown in Fig. 6(b). We can show this analytically, and thus comment on the fact that $\phi_a \leq 1$ even in the extreme and unrealistic case of ϕ_f approaching unity. Considering the upper bound $M = \sqrt{e}\,\phi_c^2/(2\bar{\sigma})$ from (30), and expressing $\bar{\sigma} = \alpha\,\phi_f$, (28) becomes:

$$\phi_a = \phi_f \left[1 + \frac{\phi_c^2 e}{2\alpha^2 \phi_f^2} e^{-1/(2\alpha^2)}\right]. \tag{31}$$

For realistic parameter values and as ϕ_f approaches unity, $\alpha \ll 1$, making the exponential term negligible so that $\phi_a \to \phi_f$. Even for finite α values, such as $\alpha = 0.1$, the exponential term is of order 10^{-20}; for $\alpha = 0.2$, it is of order 10^{-4}. Therefore, we conclude that ϕ_a remains bounded by unity throughout the physically meaningful range.

4.3. Strain energy functions for CNTs in non-agglomerated and agglomerated regions

The form of the total SEF, incorporating three additive contributions, is given in (5). Here, we define the expressions of the strain energy functions used to model the behavior of isolated CNTs in non-agglomerated regions as well as those within agglomerates. We adopt the following forms:

$$W_n = \Phi_n \left(1 + \frac{\Phi_n}{\Phi_n^\infty}\right)^{-1}, \quad \text{with} \quad \Phi_n = \frac{3}{8} E_n \left(I_4^{4/3} - 1\right), \tag{32}$$

$$W_a = \Phi_a \left(1 + \frac{\Phi_a}{\Phi_a^\infty}\right)^{-1}, \quad \text{with} \quad \Phi_a = \frac{1}{2} E_a \left(I_4 - 1\right), \tag{33}$$

where E_n and E_a represent the effective elastic moduli of the CNT contributions[9] in non-agglomerated and agglomerated regions, respectively, and $I_4 = I_1/3$. The coefficients multiplying these moduli ensure consistency with linearized elasticity in the case of randomly oriented (isotropic) CNTs, yielding the correct expression for the overall elastic modulus. In (32) and (33), the functions Φ_n and Φ_a correspond to the intact material response, while the introduction of the limiting energies Φ_n^∞ and Φ_a^∞ incorporates the effect of detachment within the framework of *continuous* softening hyperelasticity (Anssari-Benam, 2023). This will be described in detail in the following.

The exponents of I_4 in (32) and (33) are chosen differently to reflect the distinct mechanical behaviors of non-agglomerated and agglomerated CNTs, as shown in Fig. 7.[10] For W_n, the exponent $4/3$ is selected as it yields a stress–strain response consistent with the following physical interpretation. As shown in Fig. 7(a), the solid black curve captures the initial mechanical behavior in the small-strain regime, where CNTs are wavy and the stress response is governed by their gradual unpacking and reorientation. This is analogous to the response of elastomers with initially disordered molecular chains. In this regime, the tangent stiffness slightly decreases with increasing strain. At higher stretches, once the CNTs become aligned with the loading direction, the tangent stiffness increases, leading to strain hardening. Since interfacial detachment between CNTs and the matrix may eventually occur, we introduce a limiting energy Φ_n^∞, as previously mentioned. As will be described in Section 4.3.2, this limiting energy is defined as a function of a *critical strain invariant*, $I_{n,\mathrm{cr}}$. Its incorporation leads to a softening effect, as illustrated by the dashed red and blue curves.

In contrast, within agglomerates the CNTs tend to form clusters that, at the macroscopic scale, behave more like particle inclusions than individual fibers. Consequently, the exponent of I_4 in W_a is set to 1, reducing the strain energy function to a neo-Hookean form, which better captures the mechanical behavior of elastomers containing larger inclusions. By analogy, one may consider carbon black-filled elastomers, where, for moderate strains, the neo-Hookean model can effectively reproduce the material response when the filler content is significant, since strain hardening is not pronounced in this regime. This interpretation motivates the use of a neo-Hookean formulation, as shown by the black stress–strain curve in Fig. 7(b). It is worth noting that, as observed in SEM images, interfacial detachment with increasing strain occurs predominantly in the agglomerated regions. Hence, we introduce the limiting energy Φ_a^∞, defined as a function of the critical invariant $I_{a,\mathrm{cr}}$, whose softening effect is illustrated by the dashed curves. This will be further discussed in Section 4.3.2.

In the following, we present the derivation of the expressions for the effective elastic moduli, along with the underlying concepts and governing equations related to detachment, which is modeled within the framework of *continuous* softening hyperelasticity.

4.3.1. Effective elastic moduli

To define the effective elastic moduli E_n and E_a, we consider the Young's modulus E_c of the nanocomposite, formulated using a rule of mixtures that accounts for the three phases in the PNC (Wang et al., 2008):

$$E_c = (1 - \phi_f)E_m + (\phi_f - \xi\phi_a)\eta_w\eta_0\eta_n E_{\mathrm{cnt}} + \left(\xi\phi_a\right)\eta_w\eta_0\eta_a E_{\mathrm{cnt}}. \tag{34}$$

In this expression, E_{cnt} and E_m represent the Young's moduli of CNTs and the polymer matrix, respectively. The term η_0 is the orientation factor, which describes CNT alignment within the matrix and takes values of 1 for fully aligned fibers, 3/8 for randomly oriented CNTs in two dimensions, and 1/5 for random orientation in three dimensions. The parameter $\eta_w = 1 - w/l$ accounts for nanotube waviness (Omidi et al., 2010; Fisher et al., 2003; Hassanzadeh-Aghdam and Mahmoodi, 2017), where w is the bent amplitude of the nanotubes and l their length.

The parameters η_n and η_a are length efficiency factors, accounting for the effect of CNT length on load transfer in non-agglomerated and agglomerated regions, respectively. These parameters range between 0 and 1, incorporating into the model the effectiveness of load transfer through the interphase region. In this work, they are estimated using the well-established shear lag theory. Several refinements and extensions of shear lag theory exist (Gao and Li, 2005; Guo and Zhu, 2015;

[9] The elastic modulus of an individual CNT, which may be assumed as $E_{\mathrm{cnt}} = 900$ GPa, does not fully determine the stress response. Despite its high intrinsic stiffness, the nanotube-matrix interaction governs its actual contribution, requiring the use of an effective elastic modulus. Its expression will be formally defined later based on established theoretical models.

[10] The uniaxial stress–stretch relations corresponding to the CNT contributions, $\sigma_{x,n}$ and $\sigma_{x,a}$, associated with the non-agglomerated and agglomerated regions, respectively, are reported in Eq. (A.1). In Fig. 7, the case of a randomly oriented distribution of CNTs ($\kappa = 1/3$) is shown.

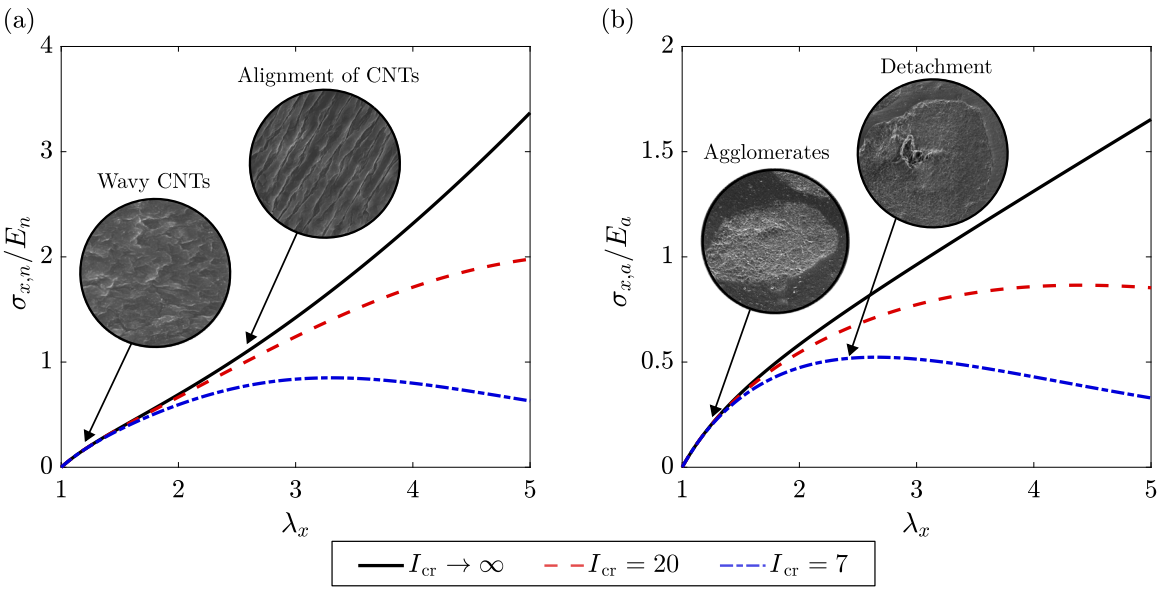

Fig. 7. Uniaxial stress σ_x vs. stretch λ_x response of CNT contributions in non-agglomerated regions ($\sigma_{x,n}$) and agglomerated regions ($\sigma_{x,a}$) under simple tension, derived from the strain energy functions in (32) and (33), respectively. (a) The solid black curve represents the response without softening ($I_{n,\rm cr} \to \infty$), characterized by an initial regime at small stretches where CNTs are wavy and progressively reorient, resulting in a slightly decreasing tangent stiffness. At higher stretches (approximately $\lambda_x = 2-2.5$), alignment of CNTs leads to a marked increase in stiffness. The dashed red and blue curves illustrate the effect of introducing softening through finite values of $I_{n,\rm cr}$, accounting for the possible detachment of CNTs from the matrix in non-agglomerated regions. (b) The contribution of CNTs within agglomerates follows a neo-Hookean-like response (solid black curve), reflecting a mechanical behavior similar to that of larger particle-like inclusions. The dashed curves represent the effect of softening due to the progressive detachment of CNTs within agglomerates, modeled via the critical invariant $I_{a,\rm cr}$.

Weerasinghe et al., 2017). Here, we adopt the widely used classical formulation (Kashyap et al., 2011; Clyne and Hull, 2019; Nairn, 1997):

$$\eta_n = 1 - \frac{\tanh(\beta_n s)}{\beta_n s}, \quad \text{with } \beta_n = \sqrt{\frac{2E_m}{E_{\rm cnt}(1+\nu_m)\ln(1/\phi_m)}}, \tag{35}$$

$$\eta_a = 1 - \frac{\tanh(\beta_a s)}{\beta_a s}, \quad \text{with } \beta_a = \sqrt{\frac{2E_m}{E_{\rm cnt}(1+\nu_m)\ln(1/\phi_a)}}, \tag{36}$$

where s is the aspect ratio of the CNTs, ν_m is the Poisson's ratio of the matrix, and ϕ_m and ϕ_a are expressed in (4) and (28), respectively.

Given these definitions, we can define the expressions for the effective elastic moduli from (34) as:

$$E_n = \eta_w \eta_0 \eta_n E_{\rm cnt}, \quad E_a = \eta_w \eta_0 \eta_a E_{\rm cnt}. \tag{37}$$

These expressions account for the effects of waviness, orientation, and nanotube-matrix load transfer efficiency.

4.3.2. Detachment of CNTs: Softening hyperelasticity

Detachment is introduced as a *continuous* softening phenomenon by requiring the strain energy to remain bounded as $I_4 \to \infty$, approaching a finite limiting value (Volokh, 2007). In Pelliciari et al. (2025), we proposed a softening energy formulation that reproduces the experimentally observed softening in elastomers caused by detachment due to the inclusion of graphene nanoplatelets. In the present work, we apply this concept to both CNT contributions, W_n and W_a, using the energy forms given in (32) and (33),[11] under the assumption that detachment may occur in both agglomerated and non-agglomerated regions. Accordingly, the intact strain energies Φ_n and Φ_a diverge as $I_4 \to \infty$, while the softening energies W_n and W_a asymptotically approach their respective limiting values, Φ_n^∞ and Φ_a^∞.

The critical advancement proposed in this work is the definition of the limiting energies associated with detachment through the introduction of *critical (detachment) strain invariants*, denoted by $I_{n,\rm cr}$ and $I_{a,\rm cr}$ for the non-agglomerated and agglomerated regions, respectively. These critical values identify the onset of detachment and are used to define the corresponding limiting strain energy expressions:

$$\Phi_n^\infty = \frac{3}{8} E_n \left(I_{n,\rm cr}^{4/3} - 1 \right), \quad \Phi_a^\infty = \frac{1}{2} E_a \left(I_{a,\rm cr} - 1 \right). \tag{38}$$

Fig. 7 shows the stress–stretch response of the material both with and without softening, as defined by the above formulation. The limiting cases $I_{n,\rm cr} \to \infty$ and $I_{a,\rm cr} \to \infty$ recover the behavior of the material without softening.

The values of the *critical strain invariants* are estimated as follows. The stretch levels at which detachment becomes dominant can be identified through SEM observations of specimens subjected to uniaxial stretching. We denote these stretch values by $\bar{\lambda}_{x,n}$ and $\bar{\lambda}_{x,a}$, corresponding to detachment in the non-agglomerated and agglomerated regions, respectively. From these values, the associated *critical strain invariants* can be computed. The detailed derivation is provided in Appendix A, and the resulting expressions are reported here for clarity (see Box I).

Remark 3. In this work, the modeling of detachment is restricted to the framework of hyperelasticity with *continuous* softening, without incorporating damage-induced inelastic effects. While detachment naturally leads to material degradation, the inclusion of damage mechanisms,

[11] The forms used here represent a special case of the general formulation proposed in Eq. (9) of Pelliciari et al. (2025), obtained by setting $\beta = 1$. This value captures the gradual softening behavior consistent with the progressive (rather than abrupt) detachment mechanisms typically observed in PNCs. Moreover, it yielded a good fit to the experimentally observed softening reported in Pelliciari et al. (2025), and is therefore held fixed in the present work to simplify the model and reduce the number of parameters requiring calibration.

$$I_{n,\mathrm{cr}} = \left[\frac{6\left(\bar{\lambda}_{x,n}^3+2\right)^2 + 4\left(\bar{\lambda}_{x,n}^3-1\right)^2 - \frac{\bar{\lambda}_{x,n}^2}{3^{1/3}}\left(\frac{\bar{\lambda}_{x,n}^3+2}{\bar{\lambda}_{x,n}}\right)^{10/3} + \frac{14}{3^{4/3}}\left(\frac{\bar{\lambda}_{x,n}^3+2}{\bar{\lambda}_{x,n}}\right)^{4/3}\left(\bar{\lambda}_{x,n}^3-1\right)^2}{5\bar{\lambda}_{x,n}^6+8\bar{\lambda}_{x,n}^3+14} \right]^{3/4}, \tag{39}$$

$$I_{a,\mathrm{cr}} = \bar{\lambda}_{x,a}^2\left(1-\frac{6}{\bar{\lambda}_{x,a}^3+2}\right)+2. \tag{40}$$

Box I.

and thus the prediction of residual strains and inelastic behavior, lies beyond the scope of the present study. Such extensions could be developed using pseudo-elastic approaches[12] (Ogden and Roxburgh, 1999; Holzapfel and Ogden, 2020b), such as those proposed by Anssari-Benam et al. (2023), Anssari-Benam and Hossain (2024), which require dedicated experimental data from cyclic loading-unloading tests to characterize the evolution of damage and permanent deformation. These aspects are left for future extensions of the model.

Remark 4. In this remark, we highlight the differences between the present approach and that adopted in our previous work (Pelliciari et al., 2025), which focused on modeling PNCs based on graphene nanoplatelets. (1) That model was not derived from microstructural observations, but rather from general phenomenological considerations. As a result, it required an articulated fitting procedure on stress–strain data, since its parameters lacked direct physical interpretation. (2) Although the softening function used in the present work is a specific case of the formulation proposed in that study, here we introduce the limiting energies Φ_n^∞ and Φ_a^∞ through the concept of *critical strain invariants* (see Eqs. (38)–(40)). This provides a clear physical interpretation and enables calibration directly from microscopy data by observing detachment. (3) Agglomeration phenomena were not considered in the earlier work. In the present model, instead, we introduce functions that link the observed microscopic growth of agglomerates to the macroscopic continuum response (see Sections 4.1 and 4.2). (4) The strain energy functions adopted in the present work for W_n and W_a, unlike the one in Pelliciari et al. (2025), are physically motivated by the microstructure and its evolution under strain. In addition, the effective elastic moduli E_n and E_a are computed from established shear-lag theory, rather than treated as fitting parameters.

4.4. Constitutive response of the matrix

The silicone matrix displays a typical elastomeric response, characterized by strain stiffening due to the progressive alignment and extension of polymer chains under deformation. To capture this behavior, a variety of hyperelastic models have been proposed in the literature. Among them, the Yeoh-Fleming model (Yeoh and Fleming, 1997) is a widely adopted formulation. The SEF is given by

$$W_m = \frac{A}{B}\left[1-e^{-B(I_1-3)}\right] - C_{10}\left(I_m-3\right)\ln\left(1-\frac{I_1-3}{I_m-3}\right), \tag{42}$$

where A, B, C_{10}, and I_m are material parameters.

This model combines features from both Yeoh's and Gent's formulations, enabling an accurate description of the material response across a broad strain range. The exponential term, governed by A and B, captures the material behavior at small strains, based on experimental observations of shear modulus evolution. The logarithmic term, involving C_{10} and the limiting invariant I_m, dominates at large strains, where it reflects the finite extensibility of polymer chains as they approach their maximum stretch.

Note that different hyperelastic models can be used for W_m, depending on the specific polymer matrix employed in the PNCs. In our case, the Yeoh-Fleming model was found to be the most suitable among the various formulations considered, which included the Carroll model (Carroll, 2011), the Yeoh model (Yeoh, 1990), the Ogden model (Ogden, 1972), and the Gent-Gent model (Gent, 1996).

Now that all terms of the proposed hyperelastic model for PNCs have been defined, we provide a summary of the contributions and governing equations in Fig. 8 for clarity. This overview concisely illustrates the structure of the complete formulation.

Remark 5. The hyperelastic model adopted for the elastomer matrix is, by nature, phenomenological. As such, experimental data on the mechanical response of the pure polymer matrix are required to calibrate the fitting parameters A, B, C_{10}, and I_m. It is important to note, however, that this calibration is a standard step in any nonlinear elastic modeling of elastomers and is not an additional requirement introduced by the PNC model. Once determined, these parameters remain fixed throughout the analysis.

4.5. Tangent moduli tensor and the linear elasticity limit

The fourth-order tangent moduli tensor is expressed by

$$\mathcal{L} = (1-\phi_f)\mathcal{L}_m + (\phi_f - \xi\phi_a)\mathcal{L}_n + \xi\phi_a\mathcal{L}_a, \tag{43}$$

where $\mathcal{L}_m$, $\mathcal{L}_n$, and $\mathcal{L}_a$ denote the contributions from the matrix, and from CNTs in the non-agglomerated and agglomerated regions, respectively. These are expressed as (Itskov, 2000; Lopez-Pamies, 2010):

$$\mathcal{L}_m = \frac{\partial^2 W_m}{\partial \mathbf{F}^2} = 4\frac{\partial^2 W_m}{\partial I_1^2}\mathbf{F}\otimes\mathbf{F} + 2\frac{\partial W_m}{\partial I_1}\mathcal{I}, \tag{44}$$

$$\mathcal{L}_n = \frac{\partial^2 W_n}{\partial \mathbf{F}^2} = \frac{4}{9}\left[\frac{\partial^2 W_n}{\partial \Phi_n^2}\left(\frac{\partial \Phi_n}{\partial I_4}\right)^2 + \frac{\partial W_n}{\partial \Phi_n}\frac{\partial^2 \Phi_n}{\partial I_4^2}\right]\mathbf{F}\otimes\mathbf{F} + \frac{2}{3}\frac{\partial W_n}{\partial \Phi_n}\frac{\partial \Phi_n}{\partial I_4}\mathcal{I}, \tag{45}$$

$$\mathcal{L}_a = \frac{\partial^2 W_a}{\partial \mathbf{F}^2} = \frac{4}{9}\left[\frac{\partial^2 W_a}{\partial \Phi_a^2}\left(\frac{\partial \Phi_a}{\partial I_4}\right)^2 + \frac{\partial W_a}{\partial \Phi_a}\frac{\partial^2 \Phi_a}{\partial I_4^2}\right]\mathbf{F}\otimes\mathbf{F} + \frac{2}{3}\frac{\partial W_a}{\partial \Phi_a}\frac{\partial \Phi_a}{\partial I_4}\mathcal{I}, \tag{46}$$

[12] In our case, a damaged SEF may be formulated by introducing a damage parameter applied to the contributions of the CNTs, as follows:

$$\mathcal{W}(I_1, I_4, \Omega) = (1-\phi_f)W_m + \Omega\left[(\phi_f - \xi\phi_a)W_n + \xi\phi_a W_a\right] + \rho(\Omega), \tag{41}$$

where $\mathcal{W}(I_1, I_4, \Omega)$ denotes the SEF of the damaged material, $\Omega \in (0,1]$ is a scalar damage parameter, and $\rho(\Omega)$ is a smooth damage energy function satisfying $\rho(1) = 0$. Alternatively, since most of the damage is expected to occur inside agglomerates, the damage parameter may be applied solely to the contribution W_a, and not to W_n.

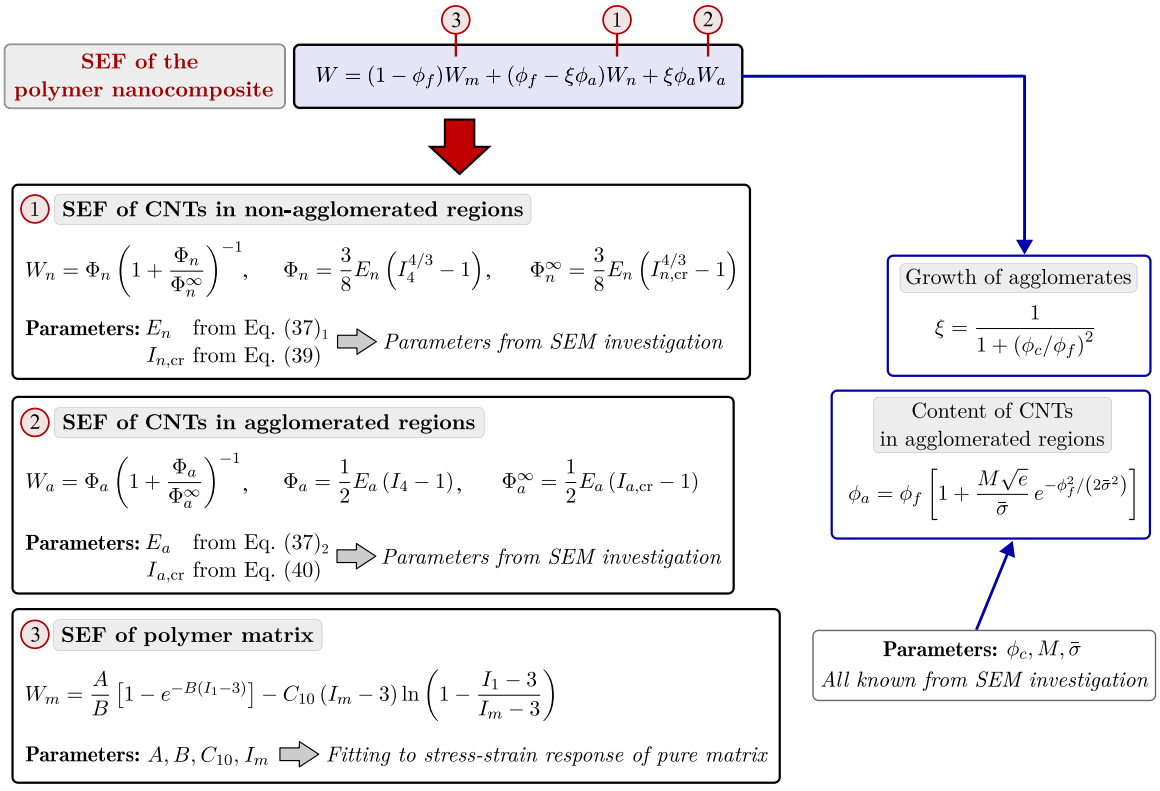

Fig. 8. Schematic representation summarizing the proposed hyperelastic modeling framework for PNCs with CNT reinforcement. The SEF consists of three distinct contributions: the non-agglomerated CNT phase (W_n), the agglomerated CNT phase (W_a), and the polymer matrix (W_m). The total volume fraction of CNTs, ϕ_f, is partitioned between non-agglomerated (ϕ_m) and agglomerated (ϕ_a) regions, with the function ξ introduced to describe the evolution of agglomeration as ϕ_f increases. The SEFs W_n and W_a each contain two parameters: the effective elastic moduli E_n and E_a, and the *critical strain invariants* $I_{n,\mathrm{cr}}$ and $I_{a,\mathrm{cr}}$, which govern the onset of softening due to detachment. These parameters are determined from SEM investigations, removing the need for empirical fitting and making the model predictive without additional experimental calibration. The polymer matrix contribution follows a phenomenological hyperelastic approach, requiring parameter fitting from the stress–strain response of the pure polymer.

where $\boldsymbol{\mathcal{I}}$ represents the fourth-order identity tensor.[13] The derivatives appearing in the above expressions can be readily computed from the definitions of the strain energy functions W_m, W_n, and W_a, given respectively in (42), (32), and (33).

To derive the expression of the Young's modulus and ensure consistency with the linear elasticity limit, we consider the tangent stiffness in uniaxial extension for the three contributions: matrix, and CNTs inside and outside the agglomerated regions. The contributions from the CNTs are defined in (A.2) and (A.3). For the incompressible matrix, under simple tension, we have that $\sigma_{x,m} = 2\,\partial W_m/\partial I_1\left(\lambda_x^3-1\right)/\lambda_x^2$, from which we can compute the derivative with respect to λ_x to obtain the tangent uniaxial stiffness. Upon evaluating these expressions in the undeformed configuration ($\lambda_x = 1$), the corresponding Young's modulus of the PNC is given by:

$$E_c = 6(1-\phi_f)\frac{\partial W_n}{\partial I_1}\bigg|_{I_1=3} + 2(\phi_f-\xi\phi_a)\frac{\partial W_n}{\partial I_4}\bigg|_{I_4=1} + 2\xi\phi_a\frac{\partial W_a}{\partial I_4}\bigg|_{I_4=1} \quad (47)$$
$$= 6\left(1-\phi_f\right)\left(A+C_{10}\right) + (\phi_f-\xi\phi_a)E_n + \xi\phi_a E_a.$$

The above result ensures that, in the proposed model, the contributions of CNTs in the small-strain regime are consistent with the rule of mixtures in linear elasticity, providing effective moduli E_n and E_a for the non-agglomerated and agglomerated regions, respectively. The matrix contribution corresponds to the Young's modulus associated with the Yeoh-Fleming model, given by $E_m = 6\left(A+C_{10}\right)$.

[13] Note that in (44), the chain rule was applied considering $W_m = W_m(I_1)$, since we are employing the Yeoh-Fleming model, which depends exclusively on the first invariant.

5. Model calibration and validation in simple tension

In this section, we calibrate the model parameters based on the results of the SEM investigation and validate the model by comparing the predicted stress response with experimental data from uniaxial tensile tests.

The microscopy analysis of bulk CNTs provided an average aspect ratio of $s = 120$ (see Fig. 2). Additionally, to estimate the parameter η_w used in the computation of the effective elastic moduli, it is necessary to assume a representative value for nanotube waviness. From the SEM images of PNC samples shown in Fig. 3, it is evident that the nanotubes exhibit some degree of waviness, though less pronounced than in their bulk state. By analyzing multiple SEM images, we estimate that the bent amplitude of the nanotubes corresponds to approximately 15% of their total length, leading to an estimated waviness parameter of $\eta_w = 0.85$.

Regarding the agglomerate content within the PNC and its increase with the overall filler volume fraction ϕ_f, it is necessary to calibrate the function ξ. Additionally, the function ϕ_a representing the CNT content in the agglomerates, where nanotubes are more densely packed, must be calibrated. To achieve this, we analyzed microscopy images and processed them using MATLAB, as detailed in Appendix B. This analysis provided parameter estimations for ξ, yielding $\phi_c = 0.037$, and for ϕ_a, with $M = 0.02$ and $\bar{\sigma} = 0.015$.

The final parameters related to the CNT contribution are the *critical strain invariants* $I_{n,\mathrm{cr}}$ and $I_{a,\mathrm{cr}}$, governing detachment in non-agglomerated and agglomerated regions, respectively. To estimate these values, we refer to the SEM investigation of stretched PNC specimens, as detailed in Section 2.2 (Fig. 4). The analysis revealed that detachment occurs entirely within agglomerates, becoming particularly

Table 1
Summary of parameters for the proposed hyperelastic model for PNCs. All parameters related to the CNT contributions were determined from microscopy investigations, while those for the polymer matrix were obtained by fitting the stress–stretch response of the pure matrix. Where applicable, units are given in MPa.

Contribution	Parameter values
Agglomeration growth function, ξ	$\phi_c = 0.037$
Content of CNTs in agglomerates, ϕ_a	$M = 0.02$, $\bar{\sigma} = 0.015$
Effective moduli, E_n and E_a	$E_{\text{cnt}} = 900 \times 10^3$, $\eta_0 = 1/5$, $\eta_w = 0.85$, $s = 120$
Detachment (softening)	$\bar{\lambda}_{x,a} = 2.5$, $\bar{\lambda}_{x,n} = 5 \rightarrow I_{a,\text{cr}} = 6.12$, $I_{n,\text{cr}} = 15.4$
Response of pure matrix, W_m	$A = -0.511$, $B = 0.163$, $C_{10} = 0.574$, $I_m = 102$ ($E_m = 0.38$, $\nu_m = 0.5$)

pronounced in the specimen subjected to a stretch of 2.5. In contrast, at this stretch level, the non-agglomerated regions showed only slight, if any, signs of detachment, indicating that softening had not yet begun in these areas.

Based on these observations, we conclude that softening in agglomerates begins at $\bar{\lambda}_{x,a} = 2.5$. For non-agglomerated regions, a clear threshold could not be identified, as visible detachment may occur at stretch levels beyond the failure point of the polymer matrix. Consequently, we reasonably assume $\bar{\lambda}_{x,n} = 5$ as the stretch at which softening would become significant in non-agglomerated regions. This assumption is reasonable, as the exact value is not critical (whether it is 5 or 6 has minimal impact on the stress–strain response, given that such high stretch levels are not even reached in our PNC specimens). Using the assumed values of $\bar{\lambda}_{x,n}$ and $\bar{\lambda}_{x,a}$ in (39) and (40), respectively, the corresponding critical strain invariants are obtained as $I_{n,\text{cr}} = 15.4$ and $I_{a,\text{cr}} = 6.12$.

Finally, the remaining parameters to be determined are those governing the SEF of the polymer matrix. As recalled, the matrix is modeled using the Yeoh-Fleming hyperelastic formulation, as given in (42). To obtain these parameters, we performed a fitting of the simple tension stress–stretch response to experimental data from uniaxial tensile tests on the silicone matrix, yielding the values $A = -0.511$ MPa, $B = 0.163$, $C_{10} = 0.574$ MPa, and $I_m = 102$. Such values correspond to a matrix Young's modulus $E_m = 6\left(A + C_{10}\right) = 0.38$ MPa.

All the calibrated parameters used in the hyperelastic model for PNCs are summarized in Table 1. It is important to note that all parameters related to the CNT contribution were determined exclusively from SEM investigations, without the need for mechanical testing.

Next, we compute the stress–stretch mechanical response of the PNCs under uniaxial tension using the calibrated parameters described above. The stress–stretch relationship under simple tension is expressed as

$$\sigma_x = (1 - \phi_f)\sigma_{x,m} + (\phi_f - \xi\phi_a)\sigma_{x,n} + \xi\phi_a\sigma_{x,a}, \tag{48}$$

where, for clarity, we recall that

$$\sigma_{x,m} = \frac{2}{\lambda_x^2}\left(\lambda_x^3 - 1\right)\frac{\partial W_m}{\partial I_1}, \quad \sigma_{x,n} = \frac{2}{3\lambda_x^2}\left(\lambda_x^3 - 1\right)\frac{\partial W_n}{\partial I_4},$$
$$\sigma_{x,a} = \frac{2}{3\lambda_x^2}\left(\lambda_x^3 - 1\right)\frac{\partial W_a}{\partial I_4}. \tag{49}$$

Fig. 9(a) shows the results for various CNT contents. The figure also includes experimental data from the simple tension tests described in Section 2.3, allowing for a direct comparison to validate the model.

First, we observe that the stress–stretch curve of the polymer matrix (black line) exhibits the typical strain stiffening behavior characteristic of elastomers. The Yeoh-Fleming model provides an accurate fit to the experimental stress–stretch response of the pure matrix. As the CNT content increases, the mechanical response becomes stiffer, as expected, and the ultimate stretch decreases. This trend is commonly observed in nanocomposites, where the introduction of CNTs leads to the formation of agglomerates and defects, which promote earlier detachment and failure.

An important observation is that, although the response is initially stiffer with increasing CNT content, the stiffening effect gradually decreases at higher stretches due to nanotube detachment. This behavior is evident in Fig. 9(b): the strain stiffening observed in the pure matrix is highly pronounced, whereas in PNCs it progressively weakens as the CNT detachment mechanism takes effect.

Overall, the model successfully predicts the uniaxial stress–stretch response of PNCs with varying CNT contents under simple tension. SEM observations provided insight into the contributions of non-agglomerated and agglomerated regions, as well as the onset of detachment. All parameters were determined accordingly, based on morphological analysis, and the resulting model accurately reproduced the observed stress–stretch behavior. In the following section, we apply the model to a three-point bending test on PNC beams.

6. Application to clamped PNC beams in three-point bending

After validating the model with simple tension experiments, we now present an application to predict the response of clamped PNC beams subjected to three-point bending. The proposed SEF was implemented in COMSOL Multiphysics to perform the simulations, and experimental measurements are presented for comparison with the numerical results.

The COMSOL model employed a 2D plane stress approximation, as shown in Fig. 10. The PNC beam had a length of $L_0 = 10.7$ cm, height $H = 1.2$ cm, and thickness $B = 1.15$ cm. Due to symmetry about the vertical midplane, we modeled only half of the beam, as shown in Fig. 10(b). As discussed later, in the experiments, a slight longitudinal prestretch was applied to straighten the beam in its initial configuration. To replicate this, a prestretch of 0.028 was imposed in COMSOL, resulting in an initial (prestretched) beam length of $L = 11$ cm. This was achieved by applying a prescribed horizontal (longitudinal) displacement at the right end of the beam. To effectively clamp this end, the vertical displacement was constrained to zero. Conversely, at the left end, vertical sliding was allowed while the horizontal displacement was fixed to zero. A vertical downward load was then applied as a boundary load over a width of $t = 0.4$ cm, simulating the contact force in the experimental setup.

The material was modeled as incompressible hyperelastic with a user-defined SEF, following the formulation for PNCs summarized in Fig. 8 and using the parameter values of Table 1. A stationary study was performed, incrementally increasing the applied load from an initial zero value to a final value in 50 steps. The resulting deformed shapes are shown in Fig. 10(c), along with a contour plot of the longitudinal stretch λ_x.

Experimental tests were conducted on PNC beams, which were glued at both ends to metallic plates. These plates were then fixed to the supports of an Instron 5567 testing machine, which applied a vertical downward displacement at the center of the beam, as shown in Fig. 11(a). The displacement was applied monotonically at a rate of 20 mm/min to ensure quasi-static conditions, and the tests were stopped upon reaching a displacement of 40 mm.

The force–displacement results from both experimental tests and FE simulations are shown in Fig. 11(b). Solid lines represent FE simulations, while dash-dotted lines correspond to experimental data. Compared to the prediction in simple tension, a slightly larger discrepancy is observed in this case, likely because the stress and strain state in this application is more complex than in simple tension. The FE model adopts a plane stress approximation of the actual conditions in the PNC

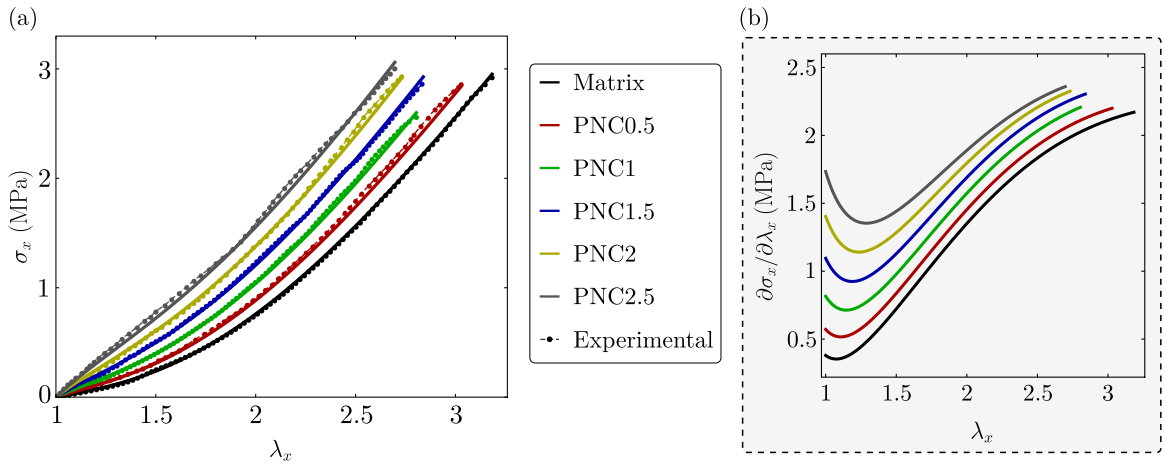

Fig. 9. Experimental results and model validation. (a) Uniaxial stress–stretch response obtained from the proposed model, compared with experimental data from simple tension tests. All model parameters were determined from microscopy investigations and are summarized in Table 1. Solid lines in different colors represent model predictions for various CNT contents, while dashed-dot lines correspond to experimental data. The CNT contents, expressed in phr, are indicated in the legend. (b) Evolution of the tangent elastic modulus, $\partial\sigma_x/\partial\lambda_x$, as a function of stretch. The initial elastic modulus increases significantly with higher CNT content. However, as stretch increases, the characteristic strain stiffening of the elastomer matrix gradually diminishes in PNCs, indicating the effect of detachment.

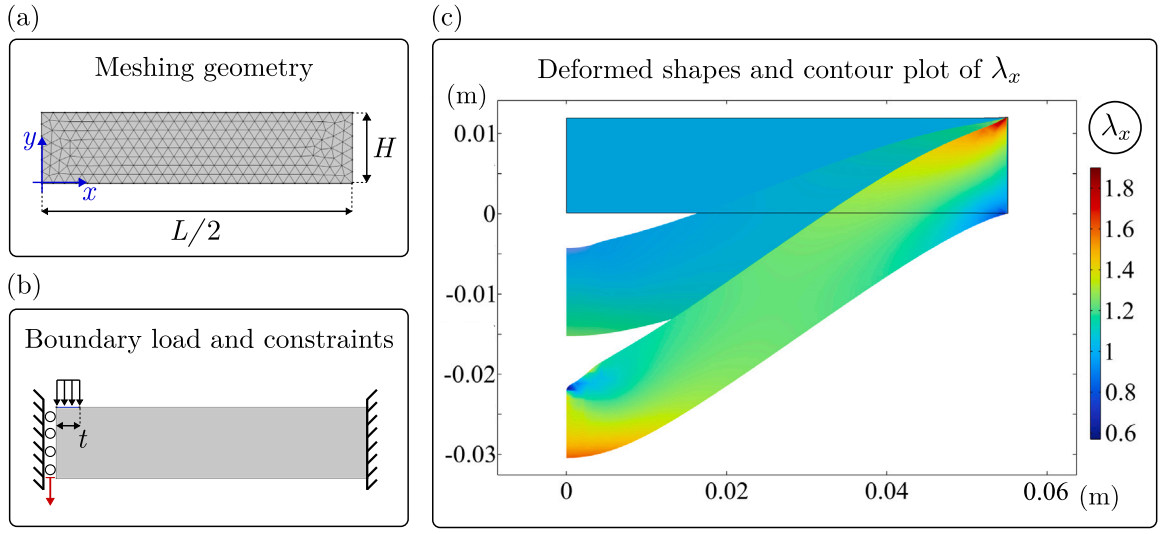

Fig. 10. FE model of a clamped PNC beam in three-point bending simulated in COMSOL. The beam has dimensions $L = 11$ cm, $H = 1.2$ cm, and $B = 1.15$ cm. (a) A 2D plane stress model is used, considering only half of the beam by exploiting symmetry along the middle vertical axis. (b) The right end is fixed, while the left end can slide vertically. A vertical boundary load is applied over a width of $t = 0.4$ cm. The material is modeled as an incompressible hyperelastic PNC with a user-defined SEF, following the formulation summarized in Fig. 8. (c) Deformed shapes and a contour plot illustrate the longitudinal stretch λ_x.

beam tests, along with additional simplifications in the loading and boundary conditions. Nevertheless, the FE simulations incorporating our proposed hyperelastic model provide a satisfactory prediction of the experimental results.

7. Simplified hyperelastic formulation: A phenomenological model

Developing a predictive model without parameter fitting requires detailed microstructural characterization, such as SEM imaging, as conducted in the present study. However, such data are not always available due to experimental limitations or the lack of access to advanced equipment. To address this issue, we propose a simplified phenomenological formulation that can be calibrated using only mechanical stress–strain data. While this approach follows a well-established tradition in solid mechanics, we aim to retain a connection to the underlying physics by ensuring that the model parameters maintain a meaningful interpretation, thereby guiding the calibration process despite the absence of direct microstructural information.

7.1. The simplified model

Each parameter of the model, as summarized in Fig. 8, has a clear physical meaning. However, some parameters, in particular M and $\bar{\sigma}$, are meaningful only when directly related to microstructural observations obtained from microscopy images. Therefore, to enable a formulation based solely on mechanical test data, we introduce a simplification. Given that the volume fraction ϕ_f in CNT-based PNCs is generally small, we linearize the expression for ϕ_a from (28). This yields the following approximation:

$$\phi_a = \phi_f \left(1 + \chi\sqrt{e}\right), \tag{50}$$

where $\chi = M/\bar{\sigma}$ is introduced as a fitting parameter. This simplification enables the calibration of a single parameter, χ, which retains a physical interpretation: it is connected to the rate at which the content of

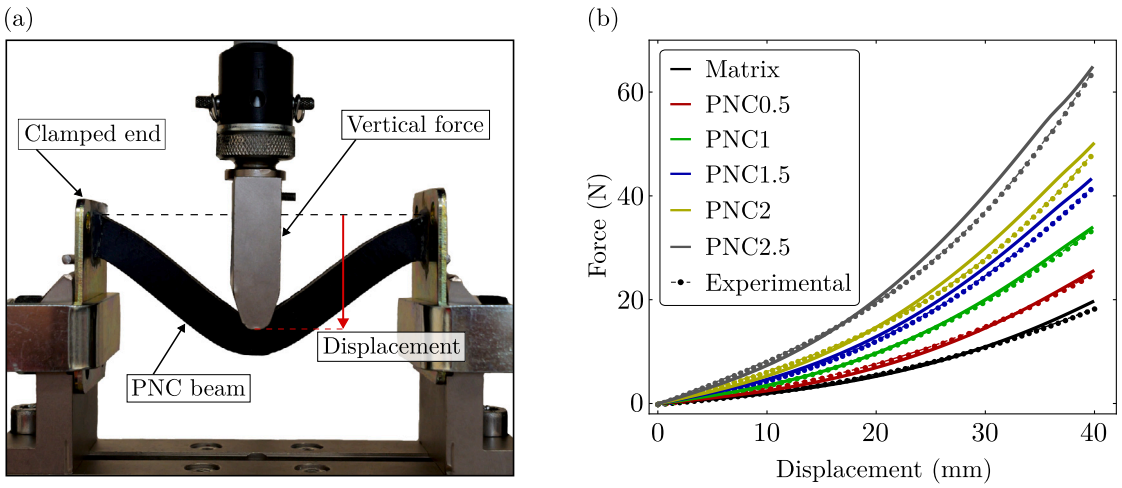

Fig. 11. Experimental tests and FE results for PNC beams under three-point bending. (a) Experimental setup for a PNC beam with a rectangular cross-section subjected to a monotonically increasing quasi-static vertical displacement. The beam is clamped at both ends by gluing it to metallic plates, which are fixed to the supports. (b) Force–displacement response, comparing experimental results (dashed and dotted lines) with FE simulations (solid lines). Different colors, as indicated in the legend, represent beams with varying CNT contents, expressed in phr.

CNTs within agglomerates increases with the total CNT volume fraction in the nanocomposite. In order to satisfy the two physical constraints discussed in Section 4.2, χ must lie within the following bounds[14]:

$$0 \le \chi \le \frac{\phi_c^2}{\phi_f^2\sqrt{e}}. \tag{51}$$

With the above definition, the form of the hyperelastic strain energy remains

$$W = (1-\phi_f)W_m + (\phi_f - \xi\phi_a)W_n + \xi\phi_a W_a, \tag{52}$$

where ξ is defined in (24), and requires fitting of the parameter ϕ_c, while ϕ_a is given by (50), which depends on the calibration of χ. The strain energy functions W_n and W_a, defined in (32) and (33), respectively, are identical in form and require only the calibration of the critical invariants $I_{n,\mathrm{cr}}$ and $I_{a,\mathrm{cr}}$, both of which have clear physical interpretations. This formulation eliminates the need for SEM imaging, allowing the model to be calibrated using mechanical test data alone, while retaining physically meaningful parameters.

Other parameters from the shear lag theory used in defining the elastic moduli in (37) also contribute. However, in practice, the only one that needs to be calibrated is the aspect ratio s. This will be clarified in the following, where we outline the calibration procedure. The main parameters to be fitted from experimental data are therefore s, ϕ_c, χ, $I_{n,\mathrm{cr}}$, and $I_{a,\mathrm{cr}}$.

What follows is a detailed description of the procedure used to calibrate the parameters of the simplified phenomenological model based on mechanical test data.

(1) Select an appropriate form for the matrix strain energy function W_m, and fit its parameters to the stress–strain data of the matrix. Additionally, estimate the value of E_m by observing its response in the small-strain regime.

(2) Set the shear lag parameters as follows: $E_{\mathrm{cnt}} = 900$ GPa, $\eta_0 = 1/5$ to account for randomly oriented CNTs, and $\eta_w = 0.85$, which is a representative value for average waviness. Next, analyze the stress–strain response of the available PNC data and calibrate the parameter s by fitting to the stiffness of the curves in the small-to-moderate strain range (e.g., stretch from 1 to 1.5). We recall that, from (48), the stress–stretch relation for the PNC in simple tension is given by

$$\sigma_x = \frac{2}{\lambda_x^2}\left(\lambda_x^3 - 1\right)\left[(1-\phi_f)\frac{\partial W_m}{\partial I_1} + \frac{1}{3}(\phi_f - \xi\phi_a)\frac{\partial W_n}{\partial I_4} + \frac{1}{3}\xi\phi_a\frac{\partial W_a}{\partial I_4}\right]. \tag{53}$$

Since s is the aspect ratio of the CNTs, it may also be provided from other sources, such as available SEM images. Note that at this stage, softening effects should not influence the model response. Therefore, the critical strain invariants are set to high values (for instance, both around 500). We also fix $\phi_c = 1$ and $\chi = 0$, excluding agglomeration effects from the response.

(3) Next, calibrate the value of $I_{n,\mathrm{cr}}$ to reproduce the trend of the experimental curves at low filler contents ϕ_f, where the response is dominated by the contribution of dispersed CNTs in the matrix and agglomeration is minimal. This calibration is guided by adjusting the reduction of strain hardening observed at large strains.

(4) Introduce the effect of agglomerate formation by setting $\chi = 1$ and reducing ϕ_c and $I_{a,\mathrm{cr}}$, calibrating these parameters to fit the experimental response at higher filler contents, where agglomerates are expected to influence the material behavior.

(5) Finally, adjust the parameter χ to refine the fit. If necessary, make small adjustments to other parameters from their previously calibrated values, while maintaining the physical consistency that guided the initial manual calibration.

In the following section, we apply the above calibration procedure to experimental data available in the literature, in order to demonstrate its applicability to large deformations of PNCs beyond those investigated in this work. For clarity, Fig. 12 provides a summary of the equations governing the simplified hyperelastic model and the associated parameters.

7.2. Calibration to experimental data available in literature

The following experimental data from uniaxial tensile tests were considered: *Dataset A*, from Frogley et al. (2003), reports data on

[14] We remind that, being a volume fraction, ϕ_a must satisfy $\phi_a \le 1$. In practice, this is never an issue, as ϕ_f is small in PNCs and thus there is no risk of ϕ_a exceeding unity. Nevertheless, one may wish to explicitly verify this even for relatively large ϕ_f to ensure physical consistency. Substituting the upper bound of χ, we obtain $\phi_a = \phi_f\left(1 + \phi_c^2/\phi_f^2\right)$, which shows that even for large ϕ_f (e.g., in the unrealistic limit $\phi_f \to 1$), the second term in parentheses is small if $\phi_c \ll 1$. As a numerical example, considering the upper limit of a plausible physical range for ϕ_f, say 0.5 to exaggerate, and assuming an (unrealistically) large value of $\phi_c = 0.4$, we obtain $\phi_a = 0.82$, which remains well below unity.

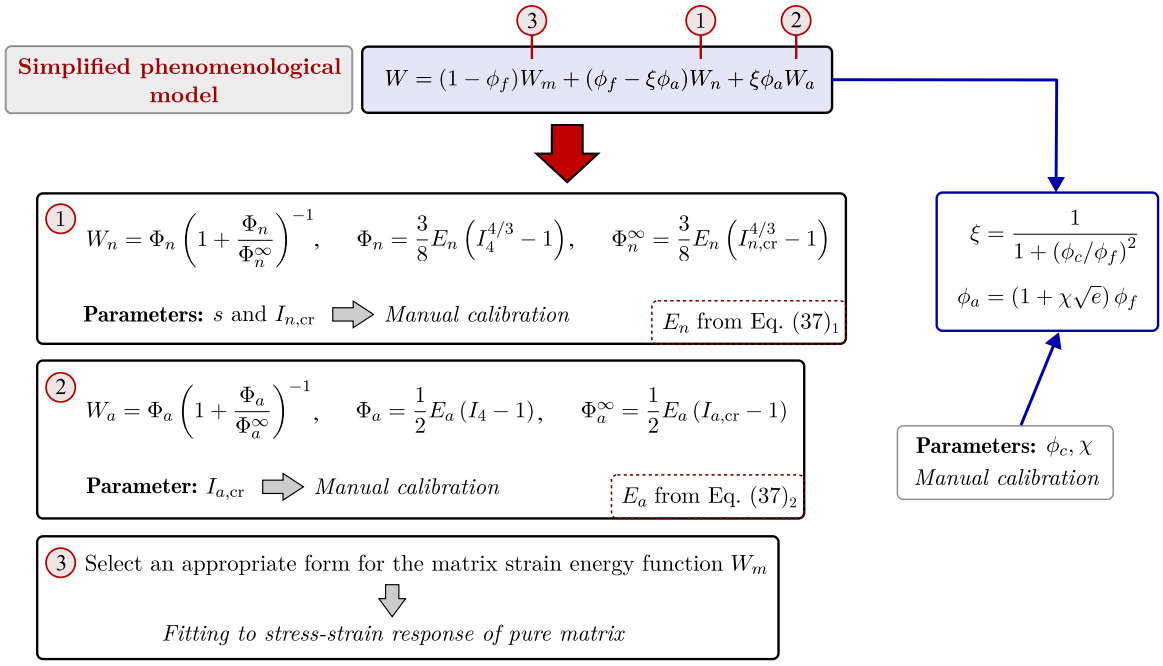

Fig. 12. Schematic representation of the proposed simplified phenomenological hyperelastic model for PNCs, designed for cases where only stress–strain data are available. The matrix contribution W_m is selected based on the specific polymer, and its parameters are fitted accordingly. Subsequently, the parameters s, ϕ_c, χ, $I_{n,\mathrm{cr}}$, and $I_{a,\mathrm{cr}}$ are manually calibrated following the procedure described in Section 7.1.

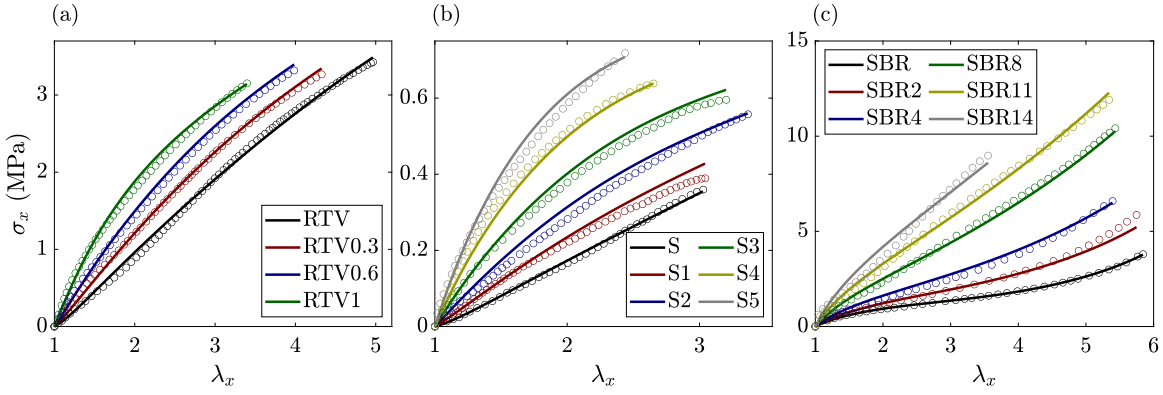

Fig. 13. Application of the simplified phenomenological model to experimental uniaxial stress–stretch data from the literature. (a) *Dataset A* by Frogley et al. (2003), (b) *Dataset B* by Alam et al. (2023), and (c) *Dataset C* by Peddini et al. (2015). Circles and solid lines represent the experimental data and model predictions, respectively. The calibrated matrix parameters are reported in Table C.2, and the parameters for the CNT contributions in Table C.3. Legends indicate the CNT content, expressed in phr.

composites made of single-walled CNTs mixed into an RTV silicone rubber matrix; *Dataset B*, presented by Alam et al. (2023), concerns RTV silicone reinforced with multi-walled CNTs; *Dataset C*, from Peddini et al. (2015), provides data on SBR rubber filled with multi-walled CNTs. The stress–stretch curves for the three datasets considered were digitized and are shown with circular markers in Fig. 13.

The datasets relate to PNCs composed of various elastomers, each exhibiting distinct behaviors that are generally not well-predicted by a single strain energy function W_m for the matrix contribution. Therefore, for each dataset, we selected a specific form of W_m that accurately fits the observed stress–stretch response of the sole matrix. This SEF of the matrix was then introduced in the total strain energy of the PNC.

In the following, we describe the strain energy functions selected for the elastomeric matrices of each dataset considered.

- The stress–stretch curve of the RTV silicone in Dataset A, shown in Fig. 13(a), exhibits mild strain stiffening at moderate stretches, followed by softening before failure. To capture this behavior, we use the Mooney–Rivlin model with softening proposed by Volokh (2007), expressed as

$$W_m = \Phi_v - \Phi_v e^{-[C_{10}(I_1-3)+C_{01}(I_2-3)]/\Phi_v}, \tag{54}$$

where C_{10} and C_{01} are Mooney–Rivlin parameters, and Φ_v denotes the material failure energy.

- For Dataset B in Fig. 13(b), the matrix response can be well reproduced by the Mooney–Rivlin model (Dal et al., 2021):

$$W_m = C_{10}\left(I_1-3\right) + C_{01}\left(I_2-3\right). \tag{55}$$

- The matrix in Dataset C, shown in Fig. 13(c), exhibits the typical uniaxial tensile response of elastomers, with strain stiffening becoming dominant at large stretches before failure. This behavior can be effectively captured by several hyperelastic models. Here, we adopt the Yeoh-Fleming model, as used for our own silicone matrix, given by (42).

We calibrated the model parameters of the selected strain energy functions for the matrices of the three datasets. The fitting of stress $\sigma_{x,m}$ to the matrix stress–stretch data was performed using the *FindFit* function in *Wolfram Mathematica*. The fitted parameters are reported in Table C.2, and the corresponding stress–stretch curves are shown as black solid lines in Figs. 13(a), (b), and (c) for Datasets A, B, and C, respectively.

After this first step, we implemented the PNC stress expression (σ_x) from (48) in *Wolfram Mathematica* and followed points (2)–(5) of the calibration procedure described in Section 7.1, yielding the parameter values reported in Table C.3. The calibration was performed manually and the resulting stress–stretch curves are shown as solid lines in Fig. 13. For all three datasets, the model satisfactorily reproduces the experimental stress response.

8. Conclusions

The mechanical modeling of PNCs under large deformations remains a complex and partially unresolved challenge. Existing constitutive models within the framework of nonlinear elasticity often fail to capture critical aspects of material response, as they lack a clear link between microscale morphology and macroscopic mechanics. The effects of agglomeration and progressive interfacial detachment during deformation are not addressed in a comprehensive and physically consistent manner, limiting both the interpretability and predictive capability of current approaches. Moreover, the mechanical response is highly sensitive to variations in fabrication methods. This highlights the need for versatile models that can be calibrated to the specific characteristics of the PNC under consideration, for instance using data from microscopic observations such as SEM imaging.

Motivated by the above limitations, this work developed a modeling framework that links the observed microstructure to the macroscopic stress response and captures its evolution under strain. The main advancements introduced by the model are summarized as follows.

- The growth of agglomerates and the locally increased concentration of CNTs within these regions are incorporated into the hyperelastic model through functions informed by underlying statistical distributions. These functions translate morphological features observed through SEM analysis into the corresponding macroscopic mechanics.
- The contributions of CNTs inside and outside the agglomerates are described by physically motivated forms of the strain energy function, reflecting the expected behavior of both isolated and agglomerated CNTs. Furthermore, the model introduces progressive detachment within the framework of *continuous* softening hyperelasticity, using *critical strain invariants* to identify the onset of interfacial debonding between CNTs and the matrix.
- The parameters of the model have a clear physical interpretation and can be directly estimated from SEM observations. This makes the model fully predictive, without requiring mechanical test data.
- The model can be readily implemented in FE codes, as demonstrated by its application to PNC beams subjected to three-point bending. This confirms its suitability for practical use in engineering applications.

In continuum mechanics, detailed microstructural characterization using SEM imaging is not a common approach. Such data may be unavailable due to limited access to advanced equipment or a lack of specialized expertise. To address this limitation, we proposed a simplified formulation in which the model parameters can be calibrated from stress–strain data obtained through experimental tests. The parameters retain a clear physical interpretation, allowing for a straightforward manual calibration process. A step-by-step procedure was presented and applied to three stress–strain datasets from the literature, demonstrating the effectiveness and validity of the proposed simplified model.

The hyperelastic formulations presented in this work represent a significant advancement over previous studies. Nonetheless, some limitations remain. First, while we aimed to extract reliable data on agglomerate growth and CNT concentration from SEM images, our analysis relied on basic imaging techniques. This aspect could be improved in future work through the use of more advanced characterization methods. Second, model validation was limited to simple tension and three-point bending tests. Future studies will consider additional loading conditions, such as biaxial stress states in PNC membranes, which are relevant for various technological applications.

CRediT authorship contribution statement

Matteo Pelliciari: Writing – review & editing, Writing – original draft, Validation, Software, Resources, Methodology, Investigation, Formal analysis, Data curation, Conceptualization. **Stefano Sirotti:** Writing – review & editing, Methodology, Investigation. **Angelo Marcello Tarantino:** Funding acquisition.

Declaration of competing interest

The authors declare that they have no known competing financial interests or personal relationships that could have appeared to influence the work reported in this paper.

Acknowledgments

This work was supported by the University of Modena and Reggio Emilia, Italy through the project “FAR Dipartimentale 2024–2025” (CUP E93C24000500005). Additional support was provided by the Italian Ministry of University and Research (MUR) through the research grants FIS 2 “PNC-Gen” (CUP E53C25000440001) and FISA-2022 “Earth-Tech” (CUP E93C24000250001). Support from the National Group of Mathematical Physics (GNFM–INdAM) is also acknowledged. The authors thank Dr. Mauro Zapparoli (CIGS, University of Modena and Reggio Emilia) for his technical assistance with the SEM.

Appendix A. Critical (detachment) strain invariants

Detachment in both agglomerated and non-agglomerated regions is identified as the point where the material response transitions from stiffening to softening. Accordingly, the critical detachment point is defined as the condition at which the stress response becomes stationary.

To derive the expressions for $I_{n,\mathrm{cr}}$ and $I_{a,\mathrm{cr}}$, we first consider the stress contributions $\sigma_{x,n}$ and $\sigma_{x,a}$, associated with the terms W_n and W_a. These are evaluated under uniaxial extension with stretch λ_x applied along the preferred mean fiber direction $\boldsymbol{a}_0$, assumed to coincide with the x axis without loss of generality (see Section 3.4). The expressions are

$$\sigma_{x,n} = \frac{2}{\lambda_x^2}\left[\lambda_x^3(1-2\kappa)-\kappa\right]\frac{\partial W_n}{\partial I_4}, \quad \sigma_{x,a} = \frac{2}{\lambda_x^2}\left[\lambda_x^3(1-2\kappa)-\kappa\right]\frac{\partial W_a}{\partial I_4}. \tag{A.1}$$

We are considering a randomly oriented distribution of CNTs within the polymer matrix, and thus the case $\kappa = 1/3$. The stationarity condition requires that the first derivative of the stress with respect to the stretch vanishes. Differentiating (A.1) with respect to λ_x and setting the result to zero yields the following equations:

$$\frac{\partial \sigma_{x,n}}{\partial \lambda_x} = \frac{1}{9\lambda_x^4}\left[6\lambda_x(2+\lambda_x^3)\frac{\partial W_n}{\partial I_4} + 4(\lambda_x^3-1)^2\frac{\partial^2 W_n}{\partial I_4^2}\right] = 0, \tag{A.2}$$

$$\frac{\partial \sigma_{x,a}}{\partial \lambda_x} = \frac{1}{9\lambda_x^4}\left[6\lambda_x(2+\lambda_x^3)\frac{\partial W_a}{\partial I_4} + 4(\lambda_x^3-1)^2\frac{\partial^2 W_a}{\partial I_4^2}\right] = 0, \tag{A.3}$$

$$I_{n,\mathrm{cr}} = \left[\frac{6\left(\lambda_x^3+2\right)^2 + 4\left(\lambda_x^3-1\right)^2 - \frac{\lambda_x^2}{3^{1/3}}\left(\frac{\lambda_x^3+2}{\lambda_x}\right)^{10/3} + \frac{14}{3^{4/3}}\left(\frac{\lambda_x^3+2}{\lambda_x}\right)^{4/3}\left(\lambda_x^3-1\right)^2}{5\lambda_x^6+8\lambda_x^3+14} \right]^{3/4}, \tag{A.5}$$

$$I_{a,\mathrm{cr}} = \lambda_x^2\left(1-\frac{6}{\lambda_x^3+2}\right)+2. \tag{A.6}$$

Box II.

where

$$\begin{aligned}
\frac{\partial W_n}{\partial I_4} &= \left(\frac{\Phi_n^\infty}{\Phi_n+\Phi_n^\infty}\right)^2 \frac{\partial \Phi_n}{\partial I_4}, \\
\frac{\partial W_a}{\partial I_4} &= \left(\frac{\Phi_a^\infty}{\Phi_a+\Phi_a^\infty}\right)^2 \frac{\partial \Phi_a}{\partial I_4}, \\
\frac{\partial^2 W_n}{\partial I_4^2} &= \frac{\left(\Phi_n^\infty\right)^2}{\left(\Phi_n+\Phi_n^\infty\right)^3}\left[\left(\Phi_n+\Phi_n^\infty\right)\frac{\partial^2 \Phi_n}{\partial I_4^2} - 2\left(\frac{\partial \Phi_n}{\partial I_4}\right)^2\right], \\
\frac{\partial^2 W_a}{\partial I_4^2} &= \frac{\left(\Phi_a^\infty\right)^2}{\left(\Phi_a+\Phi_a^\infty\right)^3}\left[\left(\Phi_a+\Phi_a^\infty\right)\frac{\partial^2 \Phi_a}{\partial I_4^2} - 2\left(\frac{\partial \Phi_a}{\partial I_4}\right)^2\right],
\end{aligned} \tag{A.4}$$

and the expressions of the strain energy functions and the limiting energies are given in (32), (33), and (38). Computing the required derivatives of Φ_n and Φ_a with respect to I_4, and solving (A.2) and (A.3), we obtain the closed-form expressions for $I_{n,\mathrm{cr}}$ and $I_{a,\mathrm{cr}}$ reported in Box II.

With the above expressions, the critical invariants can be determined without the need for any fitting parameters. By identifying the stretch values $\bar{\lambda}_{x,n}$ and $\bar{\lambda}_{x,a}$, corresponding to the full detachment in the non-agglomerated and agglomerated regions, respectively, and substituting these values for λ_x into (A.5) and (A.6), the associated invariant values are obtained.

Appendix B. MATLAB imaging for agglomerates and CNT content

For this analysis, two additional PNC specimens with CNT contents of 3 and 6 phr were produced, complementing the previously studied range of 0.5 to 2.5 phr. The choice to limit mechanical testing to a maximum of 2.5 phr, as described in Section 2.3, was based on the fact that within this range, the material exhibits enhanced mechanical properties of technological interest. Beyond 2.5 phr, the increasing CNT content leads to potential inhomogeneities and defects, reducing the practical benefits for mechanical applications. However, for microscopy analysis, we extended the study to 3 and 6 phr to explore the microstructural evolution beyond the mechanically tested range. While not essential for mechanical characterization, these additional specimens provide further insight into agglomeration behavior and dispersion at higher filler concentrations.

To estimate the parameter ϕ_c of the function ξ, which models the increase in agglomerate content, an image processing technique based on color segmentation was employed. In the original image, agglomerated CNT regions were identified with red contour (Fig. B.14(a)). A MATLAB code was developed to extract the red pixels corresponding to these agglomerate areas. A logical mask was applied to detect the pixels inside the red contours, isolating the regions of interest from the rest of the image. The total area occupied by these pixels was then computed. To quantify the relative coverage of agglomerates, the total image area was determined, and the percentage of the image occupied by agglomerates was calculated as the ratio between the identified pixel area and the total image area. This approach provides an assessment of the content of CNT agglomerated regions.

This analysis was performed for all PNC specimens produced, covering CNT contents from 0.5 to 2.5 phr, as well as the additional specimens with 3 and 6 phr. The results are presented in Fig. B.15(a), where the measured data points are shown as black dots. The figure illustrates how the agglomerate content increases with increasing CNT volume fraction, ϕ_f. From these data, the parameter ϕ_c in the function ξ (Eq. (24)) was manually adjusted to fit the curve, resulting in $\phi_c = 0.037$. The corresponding fitted curve is shown in red in the figure. Additionally, an inset with a gray background is included to highlight the trend at higher ϕ_f, where the increase in agglomerate content begins to plateau.

To estimate the CNT content within the agglomerates, the original high-magnification SEM images (Fig. B.14(b)) were first converted to a normalized grayscale format to ensure consistent intensity values. A thresholding approach was then applied to generate a binary image, where pixels above a predefined intensity threshold were classified as CNT-covered regions. The threshold value was selected based on prior observations to effectively distinguish CNTs from the surrounding polymer matrix. The binary image was subsequently used to quantify the area occupied by CNTs. This was achieved by summing the number of white pixels, while the total area was determined by the total number of pixels in the image. The percentage of the area covered by CNTs was then calculated as the ratio of these values.

This analysis was conducted for all PNC specimens, and the results are presented in Fig. B.15(b), where the measured data points are shown as black dots. As expected, the CNT content increases with increasing filler concentration. However, beyond a certain point it begins to plateau, as anticipated in the discussion of Section 4.2. Specifically, after 2.5 phr (corresponding to $\phi_f \approx 0.014$), the increase becomes negligible. In fact for the specimen with 6 phr ($\phi_f \approx 0.032$), the data tend toward the dashed black line, which represents the overall average CNT content, ϕ_f. Based on these observations, the function ϕ_a given in (28) was fitted to the experimental data, yielding the red curve shown in the figure. The parameters obtained from this fit are $M = 0.02$ and $\bar{\sigma} = 0.015$.

Appendix C. Fitting parameters

Tables C.2 and C.3 report the fitted parameters for the matrix contribution W_m and the calibrated parameters for the CNT contributions W_n and W_a, respectively, corresponding to Datasets A, B, and C.

The densities of the constituent materials used in the nanocomposites, required to compute the volume fractions for the three referenced datasets, are reported below. Frogley et al. (2003) reported densities of 1.215 g/cm^3 for RTV silicone and 1.34 g/cm^3 for CNTs. For the PNCs investigated by Alam et al. (2023), the reported densities are 1.28 g/cm^3 for RTV silicone (KE-12, Shin-Etsu) and 1.74 g/cm^3 for CNTs. Lastly, for the materials analyzed by Peddini et al. (2015), the reported densities are 0.94 g/cm^3 for SBR and 1.85 g/cm^3 for CNTs. It is worth noting that for the dataset by Peddini, the aspect ratio of the CNTs is also available. Based on the morphological analysis presented in Peddini et al. (2014), the average diameter is 12.6 nm and the average length is 500 nm, yielding an estimated aspect ratio of $s \approx 40$.

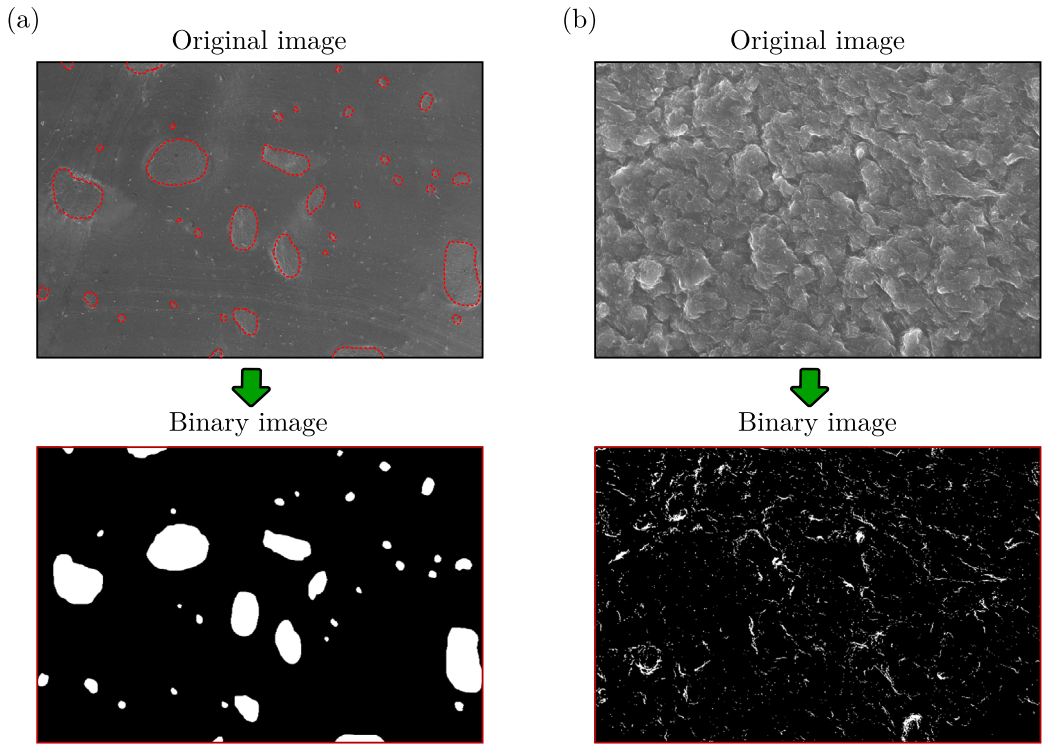

Fig. B.14. Identification of (a) agglomerated CNT regions and (b) the CNT content within agglomerates for a PNC specimen with 2 phr. In (a), the processed SEM image highlights agglomerates with a red contour, which are then extracted using a color-based segmentation approach in MATLAB. The corresponding binary image displays the identified agglomerate regions. In (b), a high-magnification SEM image of CNTs within an agglomerate is imported into MATLAB, where an intensity-based thresholding method is applied to identify the area covered by CNTs. The resulting binary images enable the quantification of both the agglomerate content and the CNT content within the agglomerates.

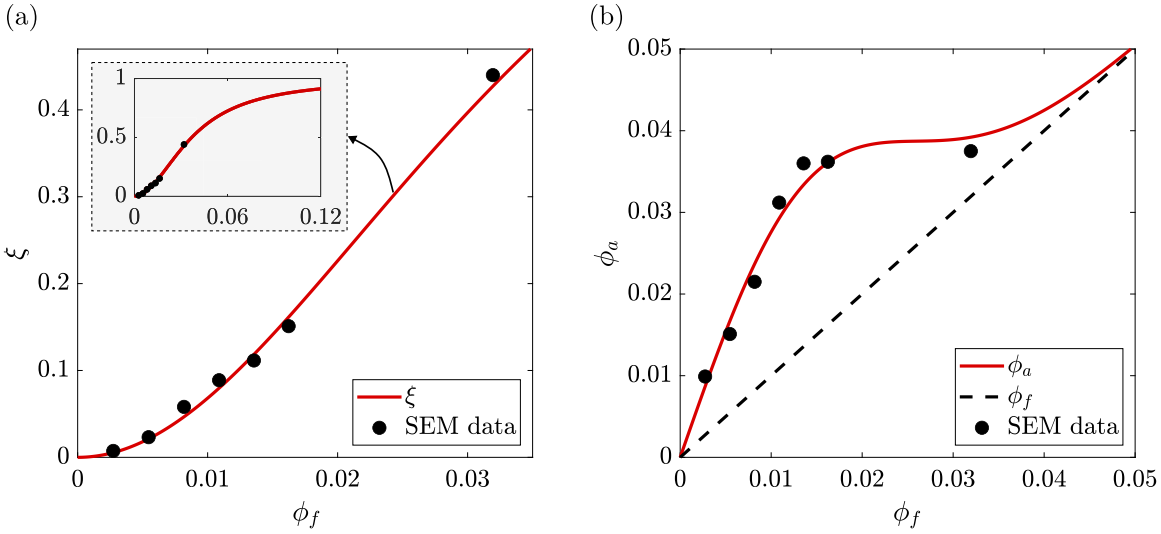

Fig. B.15. Data from SEM images and fitted functions for (a) the agglomerated CNT content, ξ, as a function of increasing ϕ_f, and (b) the CNT content inside agglomerates, ϕ_a, as a function of increasing ϕ_f. The black dots represent the data extracted from SEM images using MATLAB-based image processing. In (a), the red curve corresponds to the fitted function ξ, obtained with the parameter $\phi_c = 0.037$. The inset with a gray background provides a view of the function for a larger range of ϕ_f values, highlighting how the agglomerate content saturates at higher concentrations. In (b), the red curve represents the fitted function ϕ_a, using the parameters $M = 0.02$ and $\bar{\sigma} = 0.015$. The CNT content inside agglomerates increases with ϕ_f but eventually plateaus. At high concentrations, ϕ_a asymptotically approaches the overall average content ϕ_f (black dashed line).

The Young's modulus E_m of the matrix for the three datasets was estimated by manually fitting a linear trend to the experimental data in the small strain regime (approximately in the stretch range 1 to 1.2). The resulting approximate values are: 0.85 MPa for RTV silicone in Dataset A, 0.12 MPa for RTV silicone in Dataset 2, and 1.6 MPa for SBR in Dataset C.

Data availability

Data will be made available on request.

Table C.2
Fitted parameters for the matrix contribution W_m, based on stress–stretch response data from the literature: Dataset A (Frogley et al., 2003), Dataset B (Alam et al., 2023), and Dataset C (Peddini et al., 2015). Where applicable, values are expressed in MPa.

Dataset	Material	Model	Parameters
Dataset A	RTV silicone	Mooney–Rivlin with softening	$C_{10} = 0.461$ $C_{01} = -0.369$ $\Phi_v = 85.9$ $E_m = 0.85$
Dataset B	RTV silicone	Mooney–Rivlin	$C_{10} = 0.0832$ $C_{01} = -0.0676$ $E_m = 0.12$
Dataset C	SBR	Yeoh-Fleming	$A = 0.116$ $B = 0.167$ $C_{10} = 0.178$ $I_m = 73$ $E_m = 1.6$

Table C.3
Fitted parameters for the CNT contributions W_n and W_a, based on stress–stretch curves at varying CNT contents from experimental data reported in the literature: Dataset A (Frogley et al., 2003), Dataset B (Alam et al., 2023), and Dataset C (Peddini et al., 2015). Parameters are calibrated according to the procedure outlined in Section 7.1.

Dataset	Parameters				
	s	$I_{n,\mathrm{cr}}$	$I_{a,\mathrm{cr}}$	ϕ_c	χ
Dataset A	120	7.7	4.2	0.017	1.3
Dataset B	95	4.7	4	0.07	0.8
Dataset C	40	100	28	0.14	0.85

References

Abhiram, B., Ghosh, D., 2023. Influence of nanofiller agglomeration on fracture properties of polymer nanocomposite: Insights from atomistic simulation. Eng. Fract. Mech. 290, 109503.

Alam, M.N., Kumar, V., Lee, D.J., Choi, J., 2023. Synergistically toughened silicone rubber nanocomposites using carbon nanotubes and molybdenum disulfide for stretchable strain sensors. Compos. Part B: Eng. 259, 110759.

Anssari-Benam, A., 2023. Continuous softening up to the onset of failure: A hyperelastic modelling approach with intrinsic softening for isotropic incompressible soft solids. Mech. Res. Commun. 132, 104183.

Anssari-Benam, A., Akbari, R., Dargazany, R., 2023. Extending the theory of pseudo-elasticity to capture the permanent set and the induced anisotropy in the Mullins effect. Int. J. Non-Linear Mech. 156, 104500.

Anssari-Benam, A., Bucchi, A., 2021. A generalised neo-Hookean strain energy function for application to the finite deformation of elastomers. Int. J. Non-Linear Mech. 128, 103626.

Anssari-Benam, A., Hossain, M., 2024. A unified pseudo-elastic model of continuous and discontinuous softening in the finite deformation of isotropic soft solids. Int. J. Solids Struct. 290, 112670.

Arash, B., Exner, W., Rolfes, R., 2019. A viscoelastic damage model for nanoparticle/epoxy nanocomposites at finite strain: A multiscale approach. J. Mech. Phys. Solids 128, 162–180.

Arash, B., Unger, R., Exner, W., Rolfes, R., 2021. A finite deformation gradient-enhanced damage model for nanoparticle/polymer nanocomposites: An atomistically-informed multiscale approach. Compos. Struct. 258, 113211.

Azimi, N., Sharifzadeh, E., 2025. Improved aggregation/agglomeration-dependent percolation theory to predict nanoparticle-aided electrical conductivity in polymer nanocomposites: A combination of analytical strategy and artificial neural network. Comput. Mater. Sci. 246, 113424.

Barghamadi, M., Ghoreishy, M.H.R., Karrabi, M., Mohammadian-Gezaz, S., 2021. Modeling of nonlinear hyper-viscoelastic and stress softening behaviors of acrylonitrile butadiene rubber/polyvinyl chloride nanocomposites reinforced by nanoclay and graphene. Polym. Compos. 42 (2), 583–596.

Bassyouni, M., Abdel-Aziz, M., Zoromba, M.S., Abdel-Hamid, S., Drioli, E., 2019. A review of polymeric nanocomposite membranes for water purification. J. Ind. Eng. Chem. 73, 19–46.

Cai, R., Holweck, F., Feng, Z.Q., Peyraut, F., 2016. A new hyperelastic model for anisotropic hyperelastic materials with one fiber family. Int. J. Solids Struct. 84, 1–16.

Cantournet, S., Boyce, M.C., Tsou, A.H., 2007. Micromechanics and macromechanics of carbon nanotube-enhanced elastomers. J. Mech. Phys. Solids 55 (6), 1321–1339.

Carroll, M.M., 2011. A strain energy function for vulcanized rubbers. J. Elasticity 103, 173–187.

Cha, J., Jun, G.H., Park, J.K., Kim, J.C., Ryu, H.J., Hong, S.H., 2017. Improvement of modulus, strength and fracture toughness of CNT/Epoxy nanocomposites through the functionalization of carbon nanotubes. Compos. Part B: Eng. 129, 169–179.

Chen, L., Chen, W., Xue, Y., Zhang, M., Chen, X., Cao, X., Zhang, Z., Li, G., Li, T., 2019. Investigation of the state transition and moving boundary in a pneumatic–hydraulic coupled dielectric elastomer actuator. J. Appl. Mech. 86 (3), 031004.

Cheng, M., Chen, W., 2003. Experimental investigation of the stress–stretch behavior of EPDM rubber with loading rate effects. Int. J. Solids Struct. 40 (18), 4749–4768.

Clyne, T.W., Hull, D., 2019. An Introduction to Composite Materials. Cambridge University Press.

Cooper, C.A., Cohen, S.R., Barber, A.H., Wagner, H.D., 2002. Detachment of nanotubes from a polymer matrix. Appl. Phys. Lett. 81 (20), 3873–3875.

Cortes, D.H., Elliott, D.M., 2014. Accurate prediction of stress in fibers with distributed orientations using generalized high-order structure tensors. Mech. Mater. 75, 73–83.

Corzo, D., Tostado-Blázquez, G., Baran, D., 2020. Flexible electronics: status, challenges and opportunities. Front. Electron. 1, 594003.

Cui, Y., Kundalwal, S.I., Kumar, S., 2016. Gas barrier performance of graphene/polymer nanocomposites. Carbon 98, 313–333.

Dal, H., Açıkgöz, K., Badienia, Y., 2021. On the performance of isotropic hyperelastic constitutive models for rubber-like materials: A state of the art review. Appl. Mech. Rev. 73 (2).

Du Bois, P.A., Kolling, S., Koesters, M., Frank, T., 2006. Material behaviour of polymers under impact loading. Int. J. Impact Eng. 32 (5), 725–740.

Dufresne, A., Paillet, M., Putaux, J.L., Canet, R., Carmona, F., Delhaes, P., Cui, S., 2002. Processing and characterization of carbon nanotube/poly (styrene-co-butyl acrylate) nanocomposites. J. Mater. Sci. 37, 3915–3923.

Fisher, F., Bradshaw, R., Brinson, L., 2003. Fiber waviness in nanotube-reinforced polymer composites—I: Modulus predictions using effective nanotube properties. Compos. Sci. Technol. 63 (11), 1689–1703.

Flory, P., 1961. Thermodynamic relations for high elastic materials. Trans. Faraday Soc. 57, 829–838.

Frogley, M.D., Ravich, D., Wagner, H.D., 2003. Mechanical properties of carbon nanoparticle-reinforced elastomers. Compos. Sci. Technol. 63 (11), 1647–1654.

Fu, S., Sun, Z., Huang, P., Li, Y., Hu, N., 2019. Some basic aspects of polymer nanocomposites: A critical review. Nano Mater. Sci. 1 (1), 2–30.

Gao, X.L., Li, K., 2005. A shear-lag model for carbon nanotube-reinforced polymer composites. Int. J. Solids Struct. 42 (5–6), 1649–1667.

Gasser, T.C., Ogden, R.W., Holzapfel, G.A., 2006. Hyperelastic modelling of arterial layers with distributed collagen fibre orientations. J. R. Soc. Interface 3 (6), 15–35.

Genet, M., Couégnat, G., Tomsia, A.P., Ritchie, R.O., 2014. Scaling strength distributions in quasi-brittle materials from micro-to macro-scales: A computational approach to modeling nature-inspired structural ceramics. J. Mech. Phys. Solids 68, 93–106.

Gent, A.N., 1996. A new constitutive relation for rubber. Rubber Chem. Technol. 69 (1), 59–61.

Gesztelyi, R., Zsuga, J., Kemeny-Beke, A., Varga, B., Juhasz, B., Tosaki, A., 2012. The Hill equation and the origin of quantitative pharmacology. Arch. Hist. Exact Sci. 66, 427–438.

Gizzi, A., Pandolfi, A., Vasta, M., 2018. A generalized statistical approach for modeling fiber-reinforced materials. J. Engrg. Math. 109, 211–226.

Gorissen, B., Milana, E., Baeyens, A., Broeders, E., Christiaens, J., Collin, K., Reynaerts, D., De Volder, M., 2019. Hardware sequencing of inflatable nonlinear actuators for autonomous soft robots. Adv. Mater. 31 (3), 1804598.

Guimard, N.K., Gomez, N., Schmidt, C.E., 2007. Conducting polymers in biomedical engineering. Prog. Polym. Sci. 32 (8–9), 876–921.

Gültekin, O., Dal, H., Holzapfel, G.A., 2019. On the quasi-incompressible finite element analysis of anisotropic hyperelastic materials. Comput. Mech. 63, 443–453.

Guo, Z., Peng, X., Moran, B., 2006. A composites-based hyperelastic constitutive model for soft tissue with application to the human annulus fibrosus. J. Mech. Phys. Solids 54 (9), 1952–1971.

Guo, G., Zhu, Y., 2015. Cohesive-shear-lag modeling of interfacial stress transfer between a monolayer graphene and a polymer substrate. J. Appl. Mech. 82 (3), 031005.

Hassanzadeh-Aghdam, M., Mahmoodi, M., 2017. A comprehensive analysis of mechanical characteristics of carbon nanotube-metal matrix nanocomposites. Mater. Sci. Eng.: A 701, 34–44.

He, H., Zhang, Q., Zhang, Y., Chen, J., Zhang, L., Li, F., 2022. A comparative study of 85 hyperelastic constitutive models for both unfilled rubber and highly filled rubber nanocomposite material. Nano Mater. Sci. 4 (2), 64–82.

Holzapfel, G.A., Ogden, R.W., 2010. Constitutive modelling of arteries. Proc. R. Soc. A: Math. Phys. Eng. Sci. 466 (2118), 1551–1597.

Holzapfel, G.A., Ogden, R.W., 2020a. An arterial constitutive model accounting for collagen content and cross-linking. J. Mech. Phys. Solids 136, 103682.

Holzapfel, G.A., Ogden, R.W., 2020b. A damage model for collagen fibres with an application to collagenous soft tissues. Proc. R. Soc. A 476 (2236), 20190821.

Holzapfel, G.A., Ogden, R.W., 2025. Modeling the biomechanical properties of soft biological tissues: Constitutive theories. Eur. J. Mech. A Solids 112, 105634.

Islam, S., Yang, S., Kim, C.I., 2023. A multiscale continuum model for the mechanics of hyperelastic composite reinforced with nanofibers. Int. J. Solids Struct. 267, 112168.

Itskov, M., 2000. On the theory of fourth-order tensors and their applications in computational mechanics. Comput. Methods Appl. Mech. Engrg. 189 (2), 419–438.

Jiang, L., Huang, Y., Jiang, H., Ravichandran, G., Gao, H., Hwang, K., Liu, B., 2006. A cohesive law for carbon nanotube/polymer interfaces based on the van der waals force. J. Mech. Phys. Solids 54 (11), 2436–2452.

Kashyap, K., Koppad, P.G., Puneeth, K., Aniruddha Ram, H., Mallikarjuna, H., 2011. Elastic modulus of multiwalled carbon nanotubes reinforced aluminium matrix nanocomposite – A theoretical approach. Comput. Mater. Sci. 50 (8), 2493–2495.

Khan, S.U., Pothnis, J.R., Kim, J.K., 2013. Effects of carbon nanotube alignment on electrical and mechanical properties of epoxy nanocomposites. Compos. Part A: Appl. Sci. Manuf. 49, 26–34.

Kim, H., Abdala, A.A., Macosko, C.W., 2010. Graphene/polymer nanocomposites. Macromolecules 43 (16), 6515–6530.

Koerner, H., Liu, W., Alexander, M., Mirau, P., Dowty, H., Vaia, R.A., 2005. Deformation–morphology correlations in electrically conductive carbon nanotube—thermoplastic polyurethane nanocomposites. Polymer 46 (12), 4405–4420.

Liu, Z., McBride, A., Sharma, B.L., Steinmann, P., Saxena, P., 2021. Coupled electro-elastic deformation and instabilities of a toroidal membrane. J. Mech. Phys. Solids 151, 104221.

Liu, N., Xue, T., Qiu, J., 2025. Multi-scale modeling of hydrogel-based concrete formed under the ambient environment and the extremely harsh environment of Mars. J. Mech. Phys. Solids 196, 105969.

Lopez-Pamies, O., 2010. A new I_1-based hyperelastic model for rubber elastic materials. Comptes Rendus Mécanique 338 (1), 3–11.

Lorenz, H., Klüppel, M., 2012. Microstructure-based modelling of arbitrary deformation histories of filler-reinforced elastomers. J. Mech. Phys. Solids 60 (11), 1842–1861.

Ma, P., Siddiqui, N.A., Marom, G., Kim, J., 2010. Dispersion and functionalization of carbon nanotubes for polymer-based nanocomposites: A review. Compos. Part A: Appl. Sci. Manuf. 41 (10), 1345–1367.

Mahmoodi, M.J., Khamehchi, M., 2024. Random distribution of interphase characteristics on the overall electro-mechanical properties of CNT piezo nanocomposite: Micromechanical modeling and Monte Carlo simulation. Probabilistic Eng. Mech. 75, 103577.

Marconnet, A.M., Yamamoto, N., Panzer, M.A., Wardle, B.L., Goodson, K.E., 2011. Thermal conduction in aligned carbon nanotube–polymer nanocomposites with high packing density. ACS Nano 5 (6), 4818–4825.

Matos, M.A., Tagarielli, V.L., Baiz-Villafranca, P.M., Pinho, S.T., 2018. Predictions of the electro-mechanical response of conductive CNT-polymer composites. J. Mech. Phys. Solids 114, 84–96.

Matveeva, A.Y., Lomov, S.V., Gorbatikh, L., 2019. Debonding at the fiber/matrix interface in carbon nanotube reinforced composites: Modelling investigation. Comput. Mater. Sci. 159, 412–419.

Melnik, A.V., Da Rocha, H.B., Goriely, A., 2015. On the modeling of fiber dispersion in fiber-reinforced elastic materials. Int. J. Non-Linear Mech. 75, 92–106.

Meunier, L., Chagnon, G., Favier, D., Orgéas, L., Vacher, P., 2008. Mechanical experimental characterisation and numerical modelling of an unfilled silicone rubber. Polym. Test. 27 (6), 765–777.

Miculescu, M., Thakur, V.K., Miculescu, F., Voicu, S.I., 2016. Graphene-based polymer nanocomposite membranes: a review. Polym. Adv. Technol. 27 (7), 844–859.

Molinari, N., Sutton, A., Mostofi, A., 2018. Mechanisms of reinforcement in polymer nanocomposites. Phys. Chem. Chem. Phys. 20 (35), 23085–23094.

Moniruzzaman, M., Winey, K.I., 2006. Polymer nanocomposites containing carbon nanotubes. Macromolecules 39 (16), 5194–5205.

Moon, D., Obrzut, J., Douglas, J.F., Lam, T., Koziol, K.K., Migler, K.B., 2014. Three dimensional cluster distributions in processed multi-wall carbon nanotube polymer composites. Polymer 55 (15), 3270–3277.

Moradi, A., Ansari, R., Hassanzadeh-Aghdam, M.K., Jamali, J., 2025. Evaluating the role of agglomerated carbon nanotubes in the effective properties of polymer nanocomposites: An efficient micromechanics-based finite element framework. Comput. Mater. Sci. 246, 113337.

Moreira, L., Fulchiron, R., Seytre, G., Dubois, P., Cassagnau, P., 2010. Aggregation of carbon nanotubes in semidilute suspension. Macromolecules 43 (3), 1467–1472.

Nairn, J.A., 1997. On the use of shear-lag methods for analysis of stress transfer in unidirectional composites. Mech. Mater. 26 (2), 63–80.

Ogden, R.W., 1972. Large deformation isotropic elasticity–on the correlation of theory and experiment for incompressible rubberlike solids. Proc. R. Soc. A 326 (1567), 565–584.

Ogden, R.W., 1978. Nearly isochoric elastic deformations: application to rubberlike solids. J. Mech. Phys. Solids 26 (1), 37–57.

Ogden, R.W., 1997. Non-Linear Elastic Deformations. Courier Corporation.

Ogden, R.W., Roxburgh, D.G., 1999. A pseudo–elastic model for the Mullins effect in filled rubber. Proc. R. Soc. Lond. Ser. A Math. Phys. Eng. Sci. 455 (1988), 2861–2877.

Omidi, M., Rokni D.T., H., Milani, A.S., Seethaler, R.J., Arasteh, R., 2010. Prediction of the mechanical characteristics of multi-walled carbon nanotube/epoxy composites using a new form of the rule of mixtures. Carbon 48 (11), 3218–3228.

Pan, J., Bian, L., 2019. A physics investigation for influence of carbon nanotube agglomeration on thermal properties of composites. Mater. Chem. Phys. 236, 121777.

Pandolfi, A., Vasta, M., 2012. Fiber distributed hyperelastic modeling of biological tissues. Mech. Mater. 44, 151–162.

Papageorgiou, D.G., Li, Z., Liu, M., Kinloch, I.A., Young, R.J., 2020. Mechanisms of mechanical reinforcement by graphene and carbon nanotubes in polymer nanocomposites. Nanoscale 12 (4), 2228–2267.

Patti, A., Russo, P., Acierno, D., Acierno, S., 2016. The effect of filler functionalization on dispersion and thermal conductivity of polypropylene/multi wall carbon nanotubes composites. Compos. Part B: Eng. 94, 350–359.

Peddini, S.K., Bosnyak, C.P., Henderson, N.M., Ellison, C.J., Paul, D.R., 2014. Nanocomposites from styrene-butadiene rubber (SBR) and multiwall carbon nanotubes (MWCNT) part 1: Morphology and rheology. Polymer 55 (1), 258–270.

Peddini, S.K., Bosnyak, C.P., Henderson, N.M., Ellison, C.J., Paul, D.R., 2015. Nanocomposites from styrene–butadiene rubber (SBR) and multiwall carbon nanotubes (MWCNT) part 2: Mechanical properties. Polymer 56, 443–451.

Pelliciari, M., Sirotti, S., Aloisio, A., Tarantino, A.M., 2025. Hyperelastic model for nonlinear elastic deformations of graphene-based polymer nanocomposites. Int. J. Solids Struct. 308, 113144.

Pelliciari, M., Sirotti, S., Tarantino, A.M., 2023. A strain energy function for large deformations of compressible elastomers. J. Mech. Phys. Solids 176, 105308.

Pelliciari, M., Tarantino, A.M., 2022. A continuum model for circular graphene membranes under uniform lateral pressure. J. Elasticity 151 (2), 273–303.

Peng, X., Guo, Z., Moran, B., 2005. An anisotropic hyperelastic constitutive model with fiber-matrix shear interaction for the human annulus fibrosus. J. Appl. Mech. 73 (5), 815–824.

Pucci, E., Saccomandi, G., 2002. A note on the Gent model for rubber-like materials. Rubber Chem. Technol. 75 (5), 839–852.

Qian, D., Dickey, E.C., Andrews, R., Rantell, T., 2000. Load transfer and deformation mechanisms in carbon nanotube-polystyrene composites. Appl. Phys. Lett. 76 (20), 2868–2870.

Qin, Y., Peng, Q., Ding, Y., Lin, Z., Wang, C., Li, Y., Xu, F., Li, J., Yuan, Y., He, X., Li, Y., 2015. Lightweight, superelastic, and mechanically flexible graphene/polyimide nanocomposite foam for strain sensor application. ACS Nano 9 (9), 8933–8941.

Rahmat, M., Hubert, P., 2011. Carbon nanotube–polymer interactions in nanocomposites: a review. Compos. Sci. Technol. 72 (1), 72–84.

Rivlin, R.S., Saunders, D., 1951. Large elastic deformations of isotropic materials VII. Experiments on the deformation of rubber. Philos. Trans. R. Soc. Lond. Ser. A Math. Phys. Sci. 243 (865), 251–288.

Romanov, V.S., Lomov, S.V., Verpoest, I., Gorbatikh, L., 2015. Stress magnification due to carbon nanotube agglomeration in composites. Compos. Struct. 133, 246–256.

Rubel, R.I., Ali, M.H., Jafor, M.A., Alam, M.M., 2019. Carbon nanotubes agglomeration in reinforced composites: A review. AIMS Mater. Sci. 6 (5), 756–780.

Sansour, C., 2008. On the physical assumptions underlying the volumetric-isochoric split and the case of anisotropy. Eur. J. Mech. A Solids 27 (1), 28–39.

Schröder, J., Neff, P., Ebbing, V., 2008. Anisotropic polyconvex energies on the basis of crystallographic motivated structural tensors. J. Mech. Phys. Solids 56 (12), 3486–3506.

Senses, E., Akcora, P., 2013. An interface-driven stiffening mechanism in polymer nanocomposites. Macromolecules 46 (5), 1868–1874.

Shen, J., Liu, J., Gao, Y., Li, X., Zhang, L., 2014. Elucidating and tuning the strain-induced non-linear behavior of polymer nanocomposites: a detailed molecular dynamics simulation study. Soft Matter 10 (28), 5099–5113.

Shi, D.L., Feng, X.Q., Huang, Y.Y., Hwang, K.C., Gao, H., 2004. The effect of nanotube waviness and agglomeration on the elastic property of carbon nanotube-reinforced composites. J. Eng. Mater. Technol. 126 (3), 250–257.

Shin, H., Choi, J., Cho, M., 2019. An efficient multiscale homogenization modeling approach to describe hyperelastic behavior of polymer nanocomposites. Compos. Sci. Technol. 175, 128–134.

Spencer, A.J.M., 1984. Constitutive theory for strongly anisotropic solids. In: Continuum Theory of the Mechanics of Fibre-Reinforced Composites. Springer, pp. 1–32.

Starr, F.W., Douglas, J.F., Glotzer, S.C., 2003. Origin of particle clustering in a simulated polymer nanocomposite and its impact on rheology. J. Chem. Phys. 119 (3), 1777–1788.

Stewart, B.G., Sitaraman, S.K., 2021. Biaxial inflation stretch test for flexible electronics. Adv. Eng. Mater. 2001503.

Teichtmeister, S., Holzapfel, G.A., 2022. A constitutive model for fibrous tissues with cross-linked collagen fibers including dispersion—With an analysis of the Poynting effect. J. Mech. Phys. Solids 164, 104911.

Thakur, V.K., Kessler, M.R., 2015. Self-healing polymer nanocomposite materials: A review. Polymer 69, 369–383.

Tomita, Y., Azuma, K., Naito, M., 2008. Computational evaluation of strain-rate-dependent deformation behavior of rubber and carbon-black-filled rubber under monotonic and cyclic straining. Int. J. Mech. Sci. 50 (5), 856–868.

Truesdell, C., Noll, W., 2004. The non-linear field theories of mechanics. In: The Non-Linear Field Theories of Mechanics. Springer Berlin Heidelberg, pp. 1–579.

Volokh, K.Y., 2007. Hyperelasticity with softening for modeling materials failure. J. Mech. Phys. Solids 55 (10), 2237–2264.

Wang, W., Ciselli, P., Kuznetsov, E., Peijs, T., Barber, A., 2008. Effective reinforcement in carbon nanotube–polymer composites. Philos. Trans. R. Soc. A: Math. Phys. Eng. Sci. 366 (1870), 1613–1626.
Wang, F., Richards, V.N., Shields, S.P., Buhro, W.E., 2014. Kinetics and mechanisms of aggregative nanocrystal growth. Chem. Mater. 26 (1), 5–21.
Wang, Q., Zhu, L., 2011. Polymer nanocomposites for electrical energy storage. J. Polym. Sci. Part B: Polym. Phys. 49 (20), 1421–1429.
Weerasinghe, A., Lu, C.T., Maroudas, D., Ramasubramaniam, A., 2017. Multiscale shear-lag analysis of stiffness enhancement in polymer–graphene nanocomposites. ACS Appl. Mater. Interfaces 9 (27), 23092–23098.
Winey, K.I., Kashiwagi, T., Mu, M., 2007. Improving electrical conductivity and thermal properties of polymers by the addition of carbon nanotubes as fillers. MRS Bull. 32 (4), 348–353.
Xing, W., Wu, J., Huang, G., Li, H., Tang, M., Fu, X., 2014. Enhanced mechanical properties of graphene/natural rubber nanocomposites at low content. Polym. Int. 63 (9), 1674–1681.
Yamaguchi, K., Busfield, J.J.C., Thomas, A.G., 2003. Electrical and mechanical behavior of filled elastomers. I. The effect of strain. J. Polym. Sci. Part B: Polym. Phys. 41 (17), 2079–2089.
Yavari, A., Goriely, A., 2021. Universal deformations in anisotropic nonlinear elastic solids. J. Mech. Phys. Solids 156, 104598.
Yeoh, O.H., 1990. Characterization of elastic properties of carbon-black-filled rubber vulcanizates. Rubber Chem. Technol. 63 (5), 792–805.
Yeoh, O.H., Fleming, P.D., 1997. A new attempt to reconcile the statistical and phenomenological theories of rubber elasticity. J. Polym. Sci. Part B: Polym. Phys. 35 (12), 1919–1931.
Zare, Y., Rhee, K.Y., Hui, D., 2017. Influences of nanoparticles aggregation/agglomeration on the interfacial/interphase and tensile properties of nanocomposites. Compos. Part B: Eng. 122, 41–46.
Zeinedini, A., Shokrieh, M.M., 2024. Agglomeration phenomenon in graphene/polymer nanocomposites: Reasons, roles, and remedies. Appl. Phys. Rev. 11 (4).
Zhang, S., Hao, A., Nguyen, N., Oluwalowo, A., Liu, Z., Dessureault, Y., Park, J.G., Liang, R., 2019. Carbon nanotube/carbon composite fiber with improved strength and electrical conductivity via interface engineering. Carbon 144, 628–638.
Zhang, W., Kang, S., Liu, X., Lin, B., Huang, Y., 2023. Experimental study of a composite beam externally bonded with a carbon fiber-reinforced plastic plate. J. Build. Eng. 71, 106522.
Zhao, H., Chen, X., Xin, C., Zhao, F., Cheng, S., Lei, M., Wang, C., Zhang, J., Chen, X., Tian, H., et al., 2025. High-sensitivity and self-powered flexible pressure sensor based on multi-scale structured piezoelectric composite. Chem. Eng. J. 164787.
Zheng, Q.S., 1994. Theory of representations for tensor functions–A unified invariant approach to constitutive equations. Appl. Mech. Rev. 47 (11), 545–587.